UNIVERSITY OF OKLAHOMA

GRADUATE COLLEGE

CFAR DETECTOR PERFORMANCE IN NONHOMOGENEOUS INTERFERENCE ENVIRONMENTS

A THESIS

SUBMITTED TO THE GRADUATE FACULTY

in partial fulfillment of the requirements for the

Degree of

MASTER OF SCIENCE

By

SAMUEL ROACH
Norman, Oklahoma
2025

CFAR DETECTOR PERFORMANCE IN
NONHOMOGENEOUS INTERFERENCE ENVIRONMENTS

A THESIS APPROVED FOR THE
SCHOOL OF ELECTRICAL AND COMPUTER ENGINEERING

BY THE COMMITTEE CONSISTING OF

Dr. Nathan Goodman, Chair

Dr. Justin Metcalf

Dr. Russell Kenney

Acknowledgments

I want to thank my family for supporting me throughout my life and educational journey. Their love, sacrifices, and constant encouragement have pushed me to pursue my goals and strive for success. To my parents, Katie and Glen Roach; my brothers, Jacob and Gabriel Roach; and my grandparents, Eugene and Sandy Roach, and Margo and Joe Hayes, I love you all and am forever grateful.

I am also grateful to the ARRC for connecting me with such a great network of people. Through the guidance and expertise of Dr. Nathan Goodman and Dr. Jessica Ruyle, I've learned so much about radar systems, signal processing, and RF hardware design over the last several years. I would also like to thank Dr. Russell Kenney and Dr. Justin Metcalf for serving on my committee. Their oversight in my work has been appreciated, as was their competition in billiards and foosball. Thank you to the friends I've made at the ARRC who have helped me manage my work-life balance through valuable discussions about coursework and research, and our *Guitar Hero*, crossword puzzle, and bouldering sessions.

Finally, I want to thank my teammate in life–my beautiful wife, Jessi Roach. Your unwavering support and encouragement have helped me to find a career path that aligns with my passions. I am so grateful to walk through life with you hand-in-hand. I love you! It would be remiss not to mention our pugs, Potato and Stewart, whose snuggles, silly noises, and playful energy have brought me constant joy.

I could not have completed this work without each of you by my side.

Table of Contents

List of Tables

List of Figures

Abstract

Wide-area search radar systems must reliably detect targets over a large region of interest while maintaining a low, constant false alarm rate. Constant false alarm rate (CFAR) detectors have been proposed in the literature, and they operate by estimating statistical parameters of interference in the received signal to calculate a threshold that maintains a constant probability of false alarm. However, the nonhomogeneous nature of surface clutter degrades CFAR detection performance, often increasing the false alarm rate and reducing the probability of target detection. In this thesis, a simulation was developed to generate data representative of that produced by a ground-based surveillance radar. The simulation includes a typical processing chain employed by radar systems, and the detection performance of several CFAR detectors, including Cell-Averaging (CA), Greatest-of-Cell-Averaging (GOCA), Smallest-of-Cell-Averaging (SOCA), and Ordered-Statistics (OS), was analyzed using the simulated radar data. The OS detector was proven to be the optimal detector of the study, as it maintained the lowest false alarm rate and the highest probability of target detection when the simulated radar data contained nonhomogeneous interference.

Chapter 1

Introduction

1.1 Motivation & Background

Target detection has been a primary application of radar systems since its inception, with uses in fields such as air traffic control and homeland defense. Radar detection systems operate by transmitting radio waves that interact with scatterers within the line of sight (LOS) of the radar's antenna beam. Because radio waves have lower frequencies than visible light waves, a radar system's operation cannot be directly observed by humans. A helpful analogy for the operation of a detection radar system is a bat using echolocation to sense its surroundings. An echolocating bat transmits a sound, an acoustic wave, and listens for echoes reflected from nearby objects to estimate their distance [1]. Similarly, radar systems transmit electromagnetic waves and receive echoes from scatterers in their LOS. The received signal, which contains both interference and possible target echoes, is sampled by the radar's receiver and processed into test statistics. The radar's detector then compares test statistics to a threshold to determine if they contain interference alone, or interference and target echo signals. Common sources of interference include thermal noise, electromagnetic interference, and echoes from non-target scatterers, referred to as clutter [2].

Test statistics are a random process due to the stochastic nature of interference and target echo signals [3]. A test statistic containing interference alone may exceed the threshold, producing a false alarm of a target detection. The magnitude of the threshold used in a hypothesis test controls the false alarm rate, or the rate at which interference-only test statistics are incorrectly hypothesized. Radar detectors are typically designed to maintain a low, constant false alarm rate to ensure that downstream radar processing systems are not overwhelmed with detections. When the statistical distribution of interference-only test statistics is known, the threshold can be analytically determined to achieve a desired false alarm rate. The distribution and statistical parameters (such as the mean or variance) for a set of test statistics are usually unknown quantities, which means that the false alarm rate is unpredictable unless the interference statistics are measured or estimated.

Constant false alarm rate (CFAR) detectors in the literature adaptively set a threshold for each hypothesis test to maintain a fixed probability of false alarm. CFAR detectors assume a homogeneous interference model, in which interference-only test statistics are exponentially distributed. The exponential distribution depends on a single parameter, and CFAR detectors estimate the parameter from a subset of training cells and compute a corresponding threshold that maintains the intended false alarm rate. However, CFAR detector performance degrades when the interference-only test statistics deviate from the exponential distribution. In particular, the roughness and nonuniform reflectivity of the Earth's surface (also known as surface clutter) often violates the assumed homogeneous interference model [4]. CFAR detector variants have been proposed to address nonhomogeneous interference, aiming to maintain both a constant false alarm rate and a high probability of target detection.

This thesis presents the development of a radar system simulation designed to generate data representative of a ground-based, mechanically steered surveillance radar. The simulation models rough surface clutter illuminated by a radar transmitting a nonlinear frequency-modulated waveform with staggered pulse transmissions. A representative processing chain is implemented in the model, which includes a matched filter, clutter filter, dynamic range compressor, and noncoherent integrator. The performance of several CFAR detector algorithms is evaluated using the simulated data to assess the impact of nonhomogeneous ground clutter on their detection performance and false alarm rates.

1.2 Thesis Outline

This work is divided into the following chapters. In Chapter 2, the operation of a surveillance radar is described. This includes discussions of the transmitted radar signal's waveform, the structure of radar measurements, the radar range equation, interference sources and target echoes in the received signal, and a typical signal processing chain. In Chapter 3, an introduction to detection theory is provided. A discussion of the likelihood ratio test is presented, and then the structure of several CFAR detectors and some relevant equations relating the threshold to the probability of false alarm are shown. In Chapter 4, the simulation of an example surveillance radar is presented. The radar data simulation is discussed and nonhomogeneous test statistics are analyzed. The CFAR detectors presented in Chapter 3 are then implemented on the test statistics to analyze the performance of each CFAR detector on the simulated nonhomogeneous radar data. In Chapter 5, the results of the work are summarized and conclusions are drawn. A discussion of future work regarding these topics is also presented.

Chapter 2

Ground-Based Surveillance Radar

2.1 Radar Waveform

Radio waves within the context of this work are narrowband signals. The transmitted radar signal, $x(t)$, is written as

$$x(t) = a(t) \cos\left(2\pi F_o t + \phi(t)\right) \tag{2.1}$$

where $a(t)$ is the signal envelope, t is the time variable in seconds, F_o is the carrier frequency in Hertz (Hz), and $\phi(t)$ is the signal phase. To adequately represent a continuous signal in a discrete form, the Nyquist sampling theorem must be satisfied [5]. According to the theorem, the minimum sampling frequency is at least twice the highest frequency component present in the signal. Radar signals with large carrier frequencies demand high sample rates, which is impractical for signal analysis and physical limitations of computer hardware. Instead, the complex envelope may be used to describe a radar signal, as it is the complex baseband representation and highlights the signal's envelope and phase without the carrier frequency term. The sample rate required to represent the radar signal can then be reduced to twice the highest frequency of the complex envelope, which is much lower than the carrier frequency for narrowband signals. The complex baseband representation of a radar signal is found by demodulating the carrier frequency of the radar signal as

$$x_B(t) = \text{LPF}\{2\ \text{exp}\ (-j2\pi F_o t)\ x(t)\} \tag{2.2}$$

where j is $\sqrt{-1}$ and LPF is an ideal low-pass filter with a cutoff frequency greater than the bandwidth of $\phi(t)$ [6]. The radar signal can be expressed in a complex exponential form as

$$x(t) = \frac{a(t)}{2}\,[\ \text{exp}\ (j(2\pi F_o t + \phi(t))) + \text{exp}\ (-j(2\pi F_o t + \phi(t)))\ ]. \tag{2.3}$$

Substituting (2.3) into (2.2), x_B reduces to

$$\begin{aligned} x_B(t) = \text{LPF}\{a(t)\ \text{exp}(-j2\pi F_o t)\ [\ &\text{exp}\ (j(2\pi F_o t + \phi(t))) \\ &+ \text{exp}\ (-j(2\pi F_o t + \phi(t)))\ ]\}, \end{aligned} \tag{2.4}$$

which simplifies further to

$$x_B(t) = a(t)[\ \text{cos}\ (\phi(t)) + j\ \text{sin}\ (\phi(t))\ ]. \tag{2.5}$$

The in-phase and quadrature components of a radar signal, $x_I(t)$ and $x_Q(t)$, are defined as

$$x_I(t) = a(t)\ \text{cos}\ (\phi(t)) \tag{2.6}$$

and

$$x_Q(t) = a(t)\ \text{sin}\ (\phi(t)), \tag{2.7}$$

and the complex envelope, $\tilde{x}(t)$, is written as

$$\tilde{x}(t) = x_I(t) + j\ x_Q(t) = a(t)\ \text{exp}\ (j\phi(t)). \tag{2.8}$$

The radar signal can be reconstructed from the complex envelope as

$$x(t) = \text{Re}\left[\tilde{x}(t)\, \text{exp}\left(j2\pi F_o t\right)\right] \tag{2.9}$$

which shows that the complex envelope retains the modulation information of the radar signal [6]. Subsequent discussions of the radar signal in this work are centered around the complex envelope of the radar signal.

The bandwidth, B, of a radar signal defines its range resolution, or how closely spaced targets may be in a radar's line of sight (LOS) to be separately distinguished. Frequency modulation (FM) and phase modulation (PM) maintain a constant signal envelope while modulating the signal phase, $\phi(t)$, to increase a radar signal's bandwidth, while amplitude modulation (AM) maintains a constant signal phase and modulates the signal envelope, $a(t)$ [6]. AM signals require linear power amplifiers for radar signal transmission, which are less efficient than the saturated power amplifiers used for FM and PM waveforms [6]. A linear power amplifier varies the output power of a radar signal, while a saturated power amplifier maintains a constant output power. FM and PM signals are more commonly used than AM signals in surveillance radar applications since the detection of a target is closely related to the energy it reflects to the radar, and AM signals with the same peak power as FM and PM signals transmit less energy over the duration of a pulse [6].

For a constant-envelope signal, the instantaneous frequency is the time derivative of the signal phase [6], written as

$$f(t) = \frac{1}{2\pi}\phi'(t) \tag{2.10}$$

where f is the instantaneous frequency at time t, $\phi(t)$ is the signal phase, and $'$ is the time derivative operator. Linear FM (LFM) pulse waveforms are radar signals with an instantaneous frequency that either "up-chirps" linearly from $-B/2$ to $B/2$ Hz or "downchirps" linearly from $B/2$ to $-B/2$ Hz during pulse transmission. An LFM waveform's complex envelope is written as

$$\tilde{x}(t) = a(t)\ \text{exp}\ \left[\mp j2\pi \left(\frac{B}{2}\right) t\ \pm\ j\pi \left(\frac{B}{T_p}\right) t^2\right],\ 0 \leq t \leq T_p \tag{2.11}$$

where B is the bandwidth in Hz and T_p is the duration of the pulse. The instantaneous frequency is therefore

$$f(t) = \mp \frac{B}{2} \pm \frac{B}{T_p} t,\ 0 \leq t \leq T_p. \tag{2.12}$$

The quantity B/T_p of (2.12) is the chirp rate of the LFM waveform, and its sign controls whether it is an up-chirp or a down-chirp. Note that the highest frequency component of the LFM pulse waveform is $B/2$ Hz, and thus an LFM pulse may be adequately represented if the sampling frequency is greater than B Hz. The in-phase and quadrature components (real and imaginary, respectively) of an up-chirp LFM are plotted in Figure 2.1.

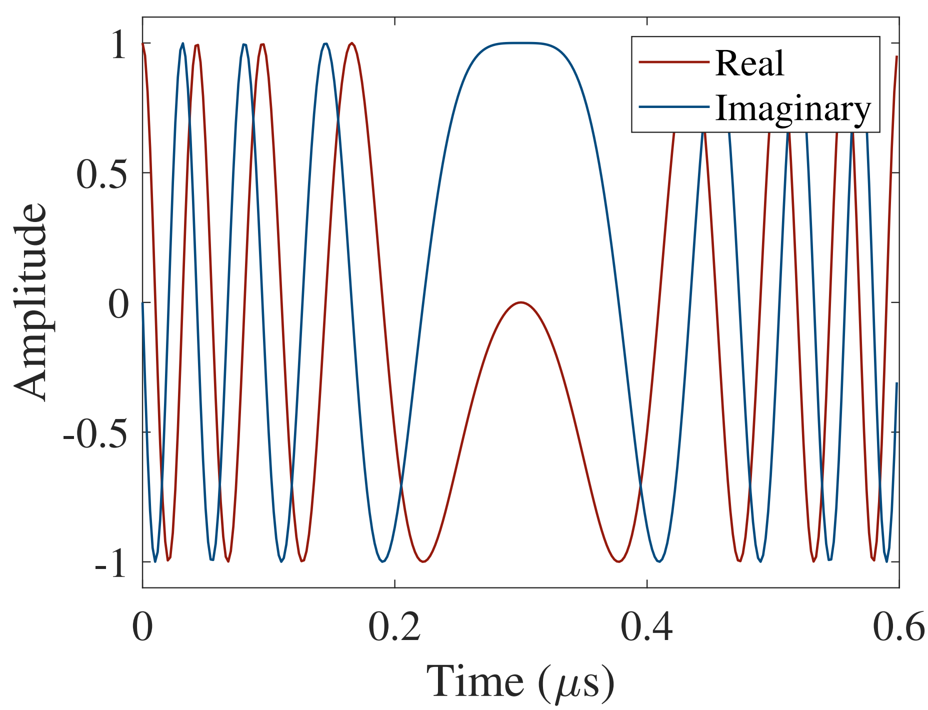

Figure 2.1: The in-phase and quadrature components of an LFM pulse waveform

A target echo signal, $s(t)$, is a time-delayed and amplitude-scaled copy of the transmitted radar signal which may be Doppler-shifted due to relative motion between the target and the radar, written as

$$s(t) = \alpha\tilde{x}(t-\tau)\,\text{exp}\,(j2\pi f_D t) \tag{2.13}$$

where α is the amplitude scale term due to propagation losses and scattering effects, τ is the time delay corresponding to the two-way propagation of the wave, and exp $(j2\pi f_D t)$ is the Doppler shift of the echo [7]. The signal received by the radar system, $r(t)$, is corrupted by interference and may contain target echo signals. In many cases, target echo are not easily distinguished in the received signal because their amplitudes are less than the interference produced by the thermal noise at the output of the receiver [6]. A filter with response $h(t)$ must be applied to the received signal that maximizes the SNR of target echo signals to ensure optimal target detection. The matched filter achieves the maximum attainable SNR when its input is the signal that the filter is matched (i.e. $\tilde{x}(t)$) and additive white noise (i.e. thermal noise) [6, 8]. The matched filter is written as the time-reversed complex conjugate of the radar signal, or

$$h(t) = \tilde{x}^*(T_p - t) \tag{2.14}$$

where T_p ensures that the matched filter is causal and * is the complex conjugate operator. An LFM pulse's matched filter is written as

$$\begin{aligned} h(t) = a^*(T_p - t)\,\text{exp}\,\left[\pm j2\pi\left(\frac{B}{2}\right)(T_p - t)\,\mp\, j\pi\left(\frac{B}{T_p}\right)(T_p - t)^2\right], \\ 0 \le t \le T_p \end{aligned} \tag{2.15}$$

which is precisely the time-reversed complex conjugate of (2.11).

The matched filter is applied to the received signal in a convolution operation as

$$y(t) = \int_{-\infty}^{\infty} r(s)h(t-s)ds \tag{2.16}$$

where $y(t)$ is the filter output, $r(t)$ is the received signal, and $h(t)$ is the matched filter response [6]. Substituting (2.14) into (2.16), the convolution operation can be rewritten as

$$y(t) = \int_{-\infty}^{\infty} r(s)\tilde{x}^*(s+T_p-t)ds = R_{\tilde{x}r}(t-T_p) \tag{2.17}$$

where the output, $y(t)$, is the cross-correlation, $R_{\tilde{x}r}(t)$, of the received signal with the complex envelope of the radar signal delayed by the duration of the pulse. Suppose that the received signal is a scaled copy of the radar signal at complex baseband, or $r(t) = \alpha\tilde{x}(t)$. Convolving the received signal with its matched filter

$$y(t) = \alpha\int_{-\infty}^{\infty} \tilde{x}(s)\tilde{x}^*(s+T_p-t)ds = R_{\tilde{x}\tilde{x}}(t-T_p) \tag{2.18}$$

the output is the autocorrelation, $R_{\tilde{x}\tilde{x}}(t)$, and its peak value at $t = T_p$ is proportional to the pulse energy as

$$y(t=T_p) = \alpha\int_{-\infty}^{\infty} |\tilde{x}(s)|^2 ds = \alpha E. \tag{2.19}$$

The autocorrelation function (ACF) of a waveform provides insight into the matched filter output when the received signal contains target echoes. The ACF of the LFM waveform from Figure 2.1 is shown in Figure 2.2 where the mainlobe and sidelobes are labeled. The width of the main lobe is inversely proportional to the waveform's bandwidth, which controls the range resolution, as previously stated. Waveforms with large bandwidths will feature a narrow mainlobe while waveforms with small bandwidths will feature a large mainlobe.

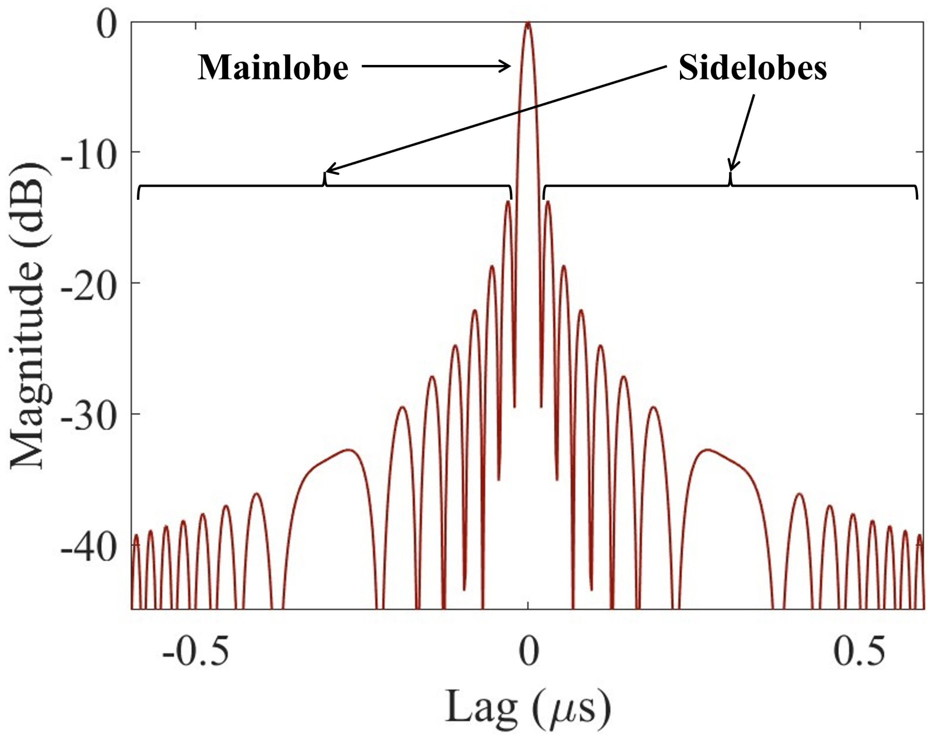

Figure 2.2: The mainlobe and sidelobes of an LFM pulse's autocorrelation function

The peaks of an LFM's ACF sidelobes are approximately 13.2 dB below the peak of the mainlobe, which may produce false alarms of target detections or mask weaker targets [2]. Windows may be applied to the radar signal in the time domain by amplitude-weighting the signal envelope to reduce the ACF sidelobes while maintaining the amplitude of the mainlobe [6]. Examples of window functions include Hann, Hamming, Kaiser, and Blackman. Time domain amplitude weighting requires a linear power amplifier (like those used in AM applications) which are less efficient than a saturated power amplifier used in constant envelope signal transmission [6]. Additionally, the energy of a windowed LFM pulse is less than the energy of a constant-envelope LFM pulse of the same peak amplitude and duration, which can negatively impact target detection.

The energy spectral density (ESD) of a waveform is the Fourier transform of its ACF, and it describes how the energy of a waveform is distributed across the frequency domain.

The Fourier transform of a function is defined as [5]

$$\mathcal{F}\{f(x)\} = \hat{f}(\psi) = \int_{-\infty}^{\infty} f(x)e^{-j2\pi\psi x}dx \quad \forall\, \psi \in \mathbb{R} \tag{2.20}$$

where $\mathcal{F}$ represents the Fourier transform. The ESD, $S(f)$, is therefore

$$S(f) = \int_{-\infty}^{\infty} R_{xx}(t)e^{-j2\pi ft}dt. \tag{2.21}$$

The sinc-like (sinc $x = \frac{\sin \pi x}{\pi x}$) nature of the LFM's ACF (Figure 2.4a) is due to its nearly rectangular ESD (Figure 2.4b), as the sinc and rectangular functions are Fourier transform pairs. An alternative approach to reducing the ACF sidelobes involves shaping the ESD of the radar signal to resemble a window function [6]. The works of Cook and Bernfeld [9] and Fowle [10] relate the ESD to the instantaneous frequency of a waveform using a stationary-phase concept, which states that the ESD at a particular frequency is relatively large if the rate of change of frequency at that time is relatively small. The stationary-phase concept can explain the rectangular nature of the LFM pulse's ESD; the constant chirp rate of an LFM waveform results in an instantaneous frequency function that allocates an equal amount of time, and therefore energy, at each frequency from $-B/2$ to $B/2$ Hz. Levanon utilizes the stationary-phase concept in a waveform design algorithm [6], where the output of the algorithm is a non-linear FM (NLFM) waveform that achieves an ESD that resembles the function at the input of the algorithm. An example NLFM waveform produced by the algorithm was presented in Levanon's work, and its ESD closely matched the input window function. However, it was shown that the matched filter output of the designed waveform was severely degraded when the input to the matched filter was not precisely the algorithm's output waveform. The waveform would therefore be disqualified for detection radar applications, as moving targets would likely go undetected due to Doppler shifts severely degrading the matched filter output. Levanon generated additional waveforms from the algorithm based on alternative window functions, but none of the waveforms showed promise for use in radar applications.

A NLFM waveform suggested by Price [11] has an instantaneous frequency function that resembles that of an LFM pulse at low frequencies, but its chirp rate increases at higher frequencies. The instantaneous frequency function of the Price NLFM waveform is written as

$$f(t) = \zeta(t)\left(B_L + \frac{B_C}{\sqrt{1-4\zeta^2(t)}}\right), 0 \leq t \leq T_p \tag{2.22}$$

where B_L is the bandwidth of the linear chirp, B_C is the bandwidth of the non-linear chirp, and $\zeta(t)$ is

$$\zeta(t) = \frac{t - \frac{T_p}{2}}{T_p} \tag{2.23}$$

The instantaneous frequency functions of an LFM pulse and Price's NLFM pulse are shown in Figure 2.3. Note that the upchirp LFM of Figure 2.1 was designed with a bandwidth of B, so this example of the Price NLFM waveform uses $B_C = B$ and $B_L = 4B$ to achieve similar instantaneous frequency functions (Figure 2.3) and ACF mainlobe widths (Figure 2.4a). The ESDs of the LFM and Price NLFM pulses are shown in Figure 2.4b; the ESD of the NLFM pulse resembles a window function whose ESD decreases as frequency increases in magnitude, while the LFM pulse's ESD is approximately rectangular across the bandwidth. The example Price NLFM waveform presents sidelobes nearly 50 dB below the mainlobe, which outperforms the LFM's sidelobes at 13.2 dB below the mainlobe.

An echo from a moving target will have a degraded filter output due to the Doppler shift mismatching the echo signal with the matched filter. The ambiguity function, $A(t; f_D)$, can be used to analyze the output of the matched filter as a function of delays and Doppler shifts

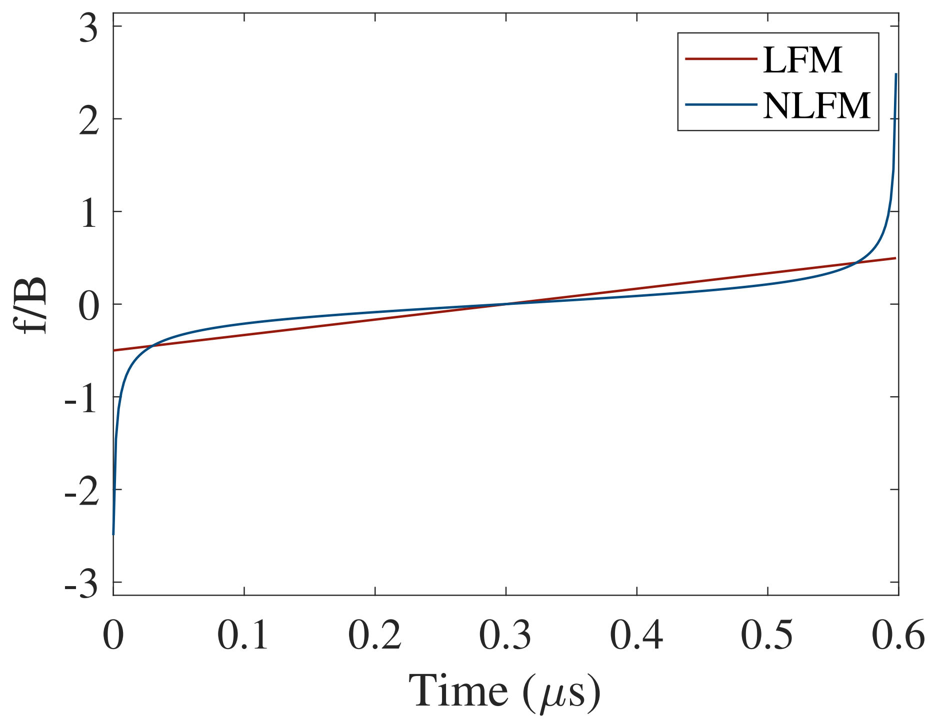

Figure 2.3: Instantaneous Frequency Functions for LFM and Price NLFM Waveforms

to the wave echo as

$$A(t; f_D) = | \int_{-\infty}^{\infty} \tilde{x}(s) \exp{(j2\pi f_D t)} \tilde{x}^*(s-t) ds | \tag{2.24}$$

which resembles the ACF with an additional Doppler term. The ambiguity function of the LFM pulse from Figure 2.1 is shown in Figure 2.5a, and the ambiguity function of the Price NLFM pulse is shown in Figure 2.5b. NLFM waveforms, such as the waveforms produced by Levanon's algorithm, are typically not Doppler tolerant, meaning that their matched filter outputs degrade severely as the Doppler shift of the wave echo is increased. The Price NLFM waveform, however, has an unusually high Doppler tolerance, as the mainlobe of the NLFM's AF in Figure 2.5b closely resembles the mainlobe of the LFM's AF in Figure 2.5a, and shows promise as a waveform to be used in detection applications.

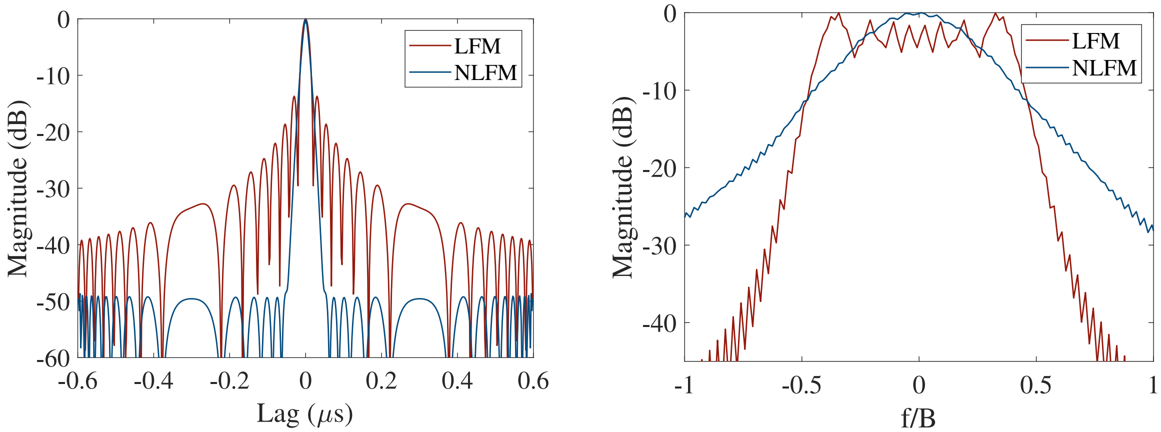

(a) ACFs (b) ESDs

Figure 2.4: ACFs and ESDs of LFM and NLFM Pulse Waveforms

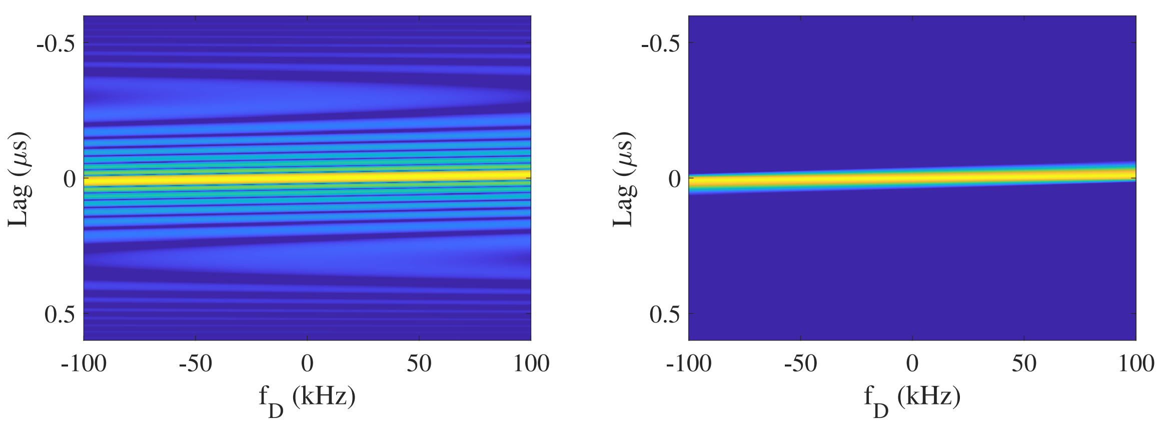

(a) LFM Pulse (b) NLFM Pulse

Figure 2.5: Ambiguity functions of LFM and Price NLFM waveforms

2.2 Radar Measurements

A radar's antenna transmits radio waves into a propagation medium, like Earth's atmosphere or free space, and the waves travel radially until they reflect from an object or medium. The radio waves reflected by targets are then sampled by the radar's receiver along with interference, such as thermal noise, clutter reflections, and electromagnetic interference, and the received signal is digitized through an analog-to-digital converter (ADC) and processed by downstream hardware. The digitized received signal are radar measurements, and they are further processed to produce test statistics that can indicate target echoes in the received signal. Figure 2.6 represents a surveillance radar sensing a target; it transmits a radar signal (the blue wave labeled "Tx") and receives an echo of the signal (the red wave labeled "Rx") after it is reflected by the green target.

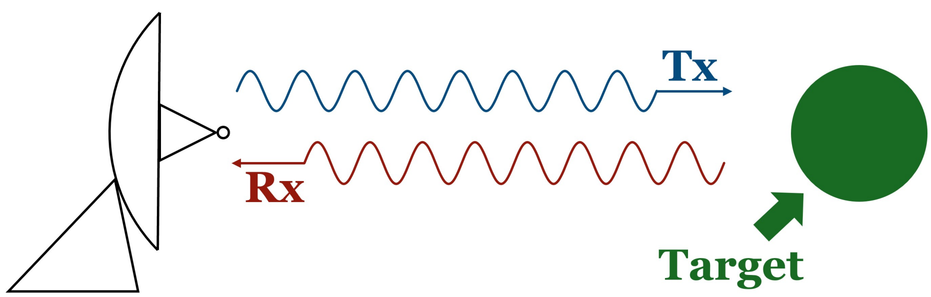

Figure 2.6: Simplified operation of a surveillance radar

Monostatic pulsed radar systems are a common architecture for ground based surveillance radars. A monostatic radar system can be designed to share the antenna for the transmitter and receiver subsystems of the radar; the receiver is composed of sensitive hardware components to detect low energy target echoes, so it is isolated from the antenna while a radio wave pulse is transmitted to prevent damage [2]. The antennas used by surveillance radars typically feature narrow beamwidths and must scan their surroundings to detect targets. Steering the antenna beam to scan a volume larger than the antenna's beamwidth may be done electrically through phased-array radar architectures or by physically rotating the antenna. The discussion of electrically steered beams is excluded from this work as the radar simulation presented in later chapters models the data produced by a mechanically steered radar system.

After a pulse of width T_p seconds is transmitted, the radar system switches from the transmit subsystem to the receive subsystem, where the ADC samples the wave echoes and interference signals before the next pulse transmission. The time delay (τ, in seconds) between a pulse transmission and when its echo returns to the radar indicates the range (R, in meters) between the radar and the reflecting object according to the following

$$\tau = \frac{2R}{c}, \tag{2.25}$$

where c is the speed of light ($c \approx 3 \cdot 10^8$ meters/second) [2]. Rearranging (2.25), the range between a reflecting object and the radar from the time delay of the pulse's two-way travel is calculated as

$$R = \frac{c\tau}{2}. \tag{2.26}$$

Substituting T_p for τ in (2.26), the minimum range at which a reflecting object can be detected after the first pulse is transmitted is at $R_{min} = cT_p/2$ meters. The minimum range is also known as the blind range, as targets closer to the radar than the minimum range cannot be detected by pulsed radar systems [2].

The time between pulse transmissions is known as the pulse repetition interval (PRI), with a reciprocal known as the pulse repetition frequency (PRF). The unambiguous range for a reflecting object, or the farthest a reflecting object can be detected before the receive subsystem is switched off for the next pulse transmission, occurs at $R_{ua} = ct_{ua}/2$ meters, where t_{ua} = PRI seconds after the beginning of the first pulse transmission. Due to scattering effects and propagation losses, the energy of an echo from a target near the unambiguous range will be less than that of a target of the same radar cross section near the minimum range. Surveillance systems implement a matched filter to correlate the received signal with the transmitted waveform to maximize SNR for optimal target detection in thermal noise [6]. Without a matched filter, a target near the unambiguous range is not likely to be distinguishable from interference. In general, the maximum range for a target detection occurs at $R_{max} = ct_{max}/2$ meters, where $t_{max} = \text{PRI} - t_{min}$ seconds after the beginning of the first pulse transmission. While targets may be detected with ranges greater than R_{max}, a target less than R_{max} and greater than R_{min} is more likely to be detected as its echo signal can be entirely correlated to the matched filter. A portion of the echo signal from a target with range greater than R_{max} would be missed by the radar after the receive subsystem was switched off, resulting in less correlation to the matched filter and consequently a weaker matched filter output.

Radar measurements between the minimum and unambiguous ranges fall into range bins, the discrete range values for radar measurements, with spacing set by the ADC sample rate and the radar's range resolution. Range resolution (ΔR) is calculated as follows

$$\Delta R = \frac{c}{2B} \tag{2.27}$$

where B is the bandwidth of the radar signal. The duration of a simple pulse is approximately the inverse of its bandwidth, but the radar signal may be modulated in amplitude or frequency to increase bandwidth. Surveillance radars often transmit FM radar signals to maintain constant output power, as discussed in Section 2.1. The sampling frequency of the ADC must meet the Nyquist sampling theorem, which states that a continuous signal must be sampled at twice the highest frequency present in the signal to be adequately represented [8]. The highest frequency of a radar signal's complex envelope is $B/2$ Hz, so the ADC sampling frequency (f_s) should be at least B Hz.

A target at range R_{min} meters in the radar's line of sight should be detected in the first radar measurement, or range bin, while a target located $R_{min} + \Delta R$ meters from the radar should be detected in the second range bin. Radar measurements may be arranged in vector format with length L corresponding to range bins R_{min} to R_{ua} with spacing ΔR. Once the L^{th} radar measurement is sampled, another pulse is transmitted. An additional L samples are collected after the second pulse is transmitted, and the data collection process is repeated until a coherent processing interval (CPI) of M pulses has been transmitted and their echoes have been sampled. The radar measurements collected on a CPI can be organized in a two-dimensional matrix of L by M samples, as shown in Figure 2.7 where each element represents a radar measurement. The first and second dimensions of the matrix are referred to as the fast-time and slow-time dimensions, respectively, because of the relative time scales between samples and pulse transmissions. The fast-time dimension of radar measurements is used to estimate a target's range, while the slow-time dimension can be used to estimate target parameters, such as its velocity or trajectory.

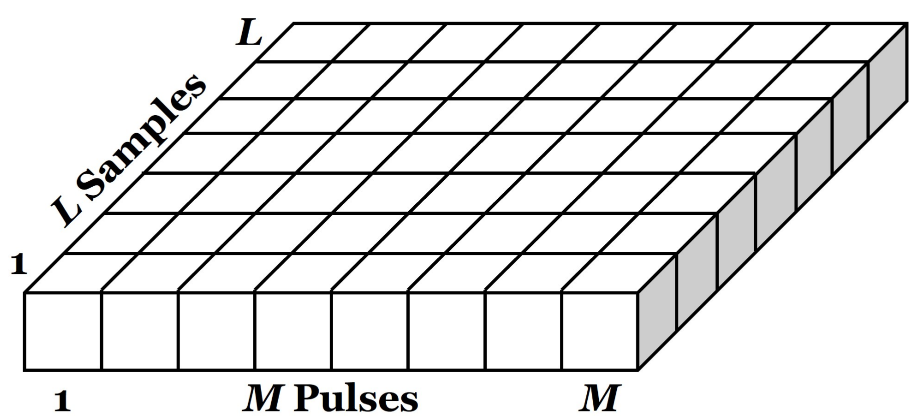

Figure 2.7: A grid of cubes that represent an L by M matrix of radar measurements

Ground based surveillance radars are often interested in the detection of non-stationary targets. Relative motion between a reflecting object and the radar shifts the frequency of the transmitted wave, which is known as a Doppler shift [2]. Assuming that the relative radial velocity (v_r) between the radar and the reflecting object is much lower than the speed of light, the Doppler shift of a waveform echo is approximately

$$f_D = \frac{2v_r}{\lambda} \tag{2.28}$$

where λ is the carrier wavelength of the transmitted radar signal [2]. The sign of the Doppler shift depends on the radial velocity; by convention, targets moving toward the radar have a positive Doppler shift, while targets moving away from the radar have a negative Doppler shift. The impact of Doppler shifts on the output of the matched filter can be analyzed the ambiguity function discussed in Section 2.1.

The Doppler shift of a moving target cannot be extracted from a single pulse by a radar system [2]. Pulse-Doppler processing converts the matrix of fast-time/slow-time radar measurements into a range-Doppler map (RDM) via the discrete Fourier transform (DFT) across slow-time measurements for every range bin, which allows for the spectral analysis of a CPI of radar measurements. The DFT is defined as

$$X_k = \sum_{m=0}^{M-1} x_m e^{-j2\pi \frac{k}{M} m} \tag{2.29}$$

where X_k is the DFT of x_m [12]. An efficient implementation of the DFT is the fast Fourier transform (FFT), which is widely used in signal processing [12]. The Doppler frequency of a moving target is sampled at the PRF of the radar system and may be estimated from the RDM. An example range-pulse map is provided in Figure 2.8a; a simulated target at range 1600 meters moving toward the radar at 1.5 meters/second is illuminated by 256 radar signal pulses. The PRF was 1 kHz, and the carrier frequency of the radar signal was 10 GHz. Converting the range-pulse map into an RDM via pulse-Doppler processing (Figure

2.8b), the target's Doppler shift is ≈ 100 Hz, as expected.

Target echo signals from a CPI of M slow-time radar measurements can achieve a SNR integration gain of M from pulse-Doppler processing due to the coherent sum of the amplitude and phase of target echo signals [2]. The integration gain of target echo signals increases the likelihood that a target is detected, so large values of M are typically chosen for the CPI of radar measurements. The dwell time, or "time-on-target," is the duration that a target is expected to be in the radar antenna's main beam [2]. The duration for which a CPI of radar measurements is collected is designed to be less than or equal to the dwell time to ensure that the target is within the radar's beam during the CPI, and the integration gain of target echo signals is approximately M. Note that the interference that corrupts the received signal is composed of thermal noise, other signals, and clutter echoes. Clutter echo signals also coherently integrate in the pulse-Doppler processing of slow-time radar measurements, resulting in the integration gain of interference power. As a result of the coherent integration of clutter echo signals, an RDM is expected to feature a strong band near zero Doppler due to clutter, as it is mostly stationary.

Pulse-Doppler processing improves the detection of moving targets outside the clutter band, as the target wave echoes do not compete with clutter echoes, but can negatively impact the detection of slow moving targets. Another range-pulse map is provided in Figure 2.9a, which features the simulated target from Figure 2.8a obscured by interference. The range-pulse map is converted to an RDM via pulse-Doppler processing, as seen in Figure 2.9b, and the target is distinguishable due to the spectral decomposition of pulse-Doppler processing. The target would likely be obscured by clutter for systems that do not implement pulse-Doppler processing, however, alternative clutter filters and non-coherent integrators, such as those used in legacy radar systems, may be implemented to achieve an integration gain of target echoes at a lower computational cost than the DFT [2].

The unambiguous velocity of a target is the maximum radial velocity a target can move

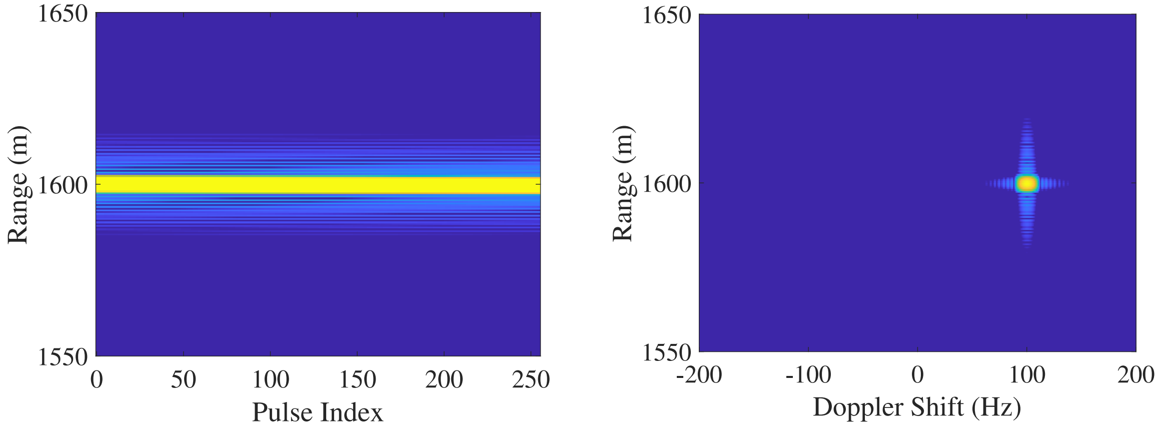

(a) Range-Pulse Map (b) Range-Doppler Map

Figure 2.8: Range-pulse and range-Doppler maps of a single target's echoes

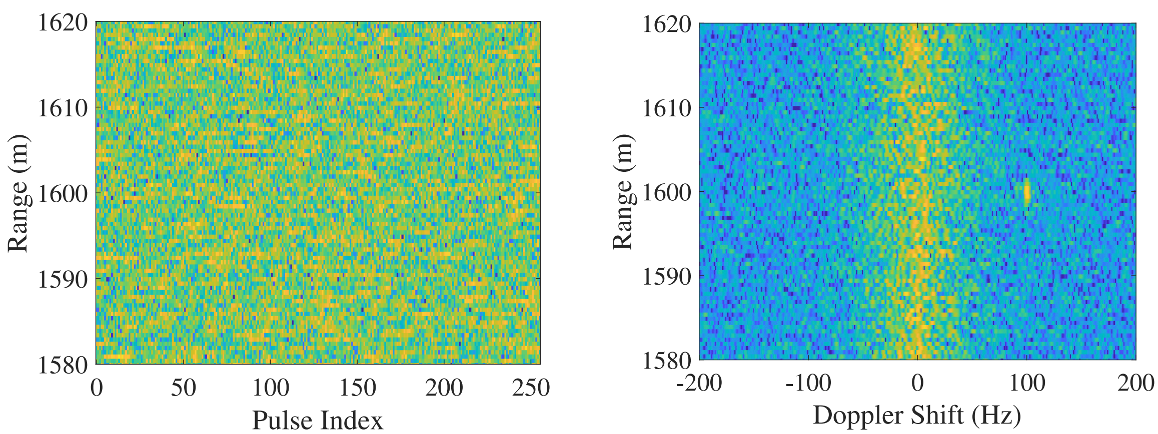

(a) Range-Pulse Map (b) Range-Doppler Map

Figure 2.9: Range-pulse and range-Doppler maps of a single target's echoes plus interference

and still be accurately located in Doppler for a CPI of radar measurements. Using the Nyquist sampling theorem, the unambiguous Doppler shift is set by the PRF as

$$f_{D,ua} = \pm\frac{PRF}{2}. \tag{2.30}$$

Rearranging (2.28), the unambiguous velocity is thus

$$v_{ua} = \pm\frac{PRF * \lambda}{4}. \tag{2.31}$$

The RDMs in Figures 2.8b and 2.9b are focused on where the target was expected to resolve, but the axes of an RDM are generally bounded from $-\frac{PRF}{2}$ to $\frac{PRF}{2}$ in the Doppler frequency dimension (or $-v_{ua}$ to v_{ua} for target velocity) and R_{min} to R_{ua} in the range dimension.

Suppose that a target is located beyond R_{ua} and its echo is received after the second pulse is transmitted. The matched filter output will result in a peak in a range bin much closer than where the target is actually positioned, which is referred to as a range ambiguity [2]. Also, suppose that another target is moving faster than the unambiguous velocity. The second target's peak will focus in a Doppler cell of the RDM that differs from its actual radial velocity due to aliasing; in some cases, a target moving toward the radar will appear as if it is moving away from the radar. A target detected by a radar moving faster than the unambiguous velocity will result in a Doppler ambiguity [2]. Range and Doppler ambiguities can result in inaccurate target detections, which are harmful to downstream systems such as tracking.

Due to the periodic nature of the DFT and discrete-time filters, clutter echoes and clutter filters with nulls at zero Doppler frequency will alias at integer multiples of the PRF. Moving targets with Doppler shifts near zero or integer multiples of the PRF are less likely to be detected, as the target echoes are likely to be attenuated by the clutter filter or embedded in the clutter band. The velocities that result in Doppler shifts near zero or integer multiples of the PRF are referred to as blind velocities due to the degraded detectability of targets [2]. The Doppler frequencies of the first blind velocities (positive and negative) are thus

$$f_b = \pm PRF \tag{2.32}$$

and the corresponding velocities are

$$v_b = \pm \frac{\lambda}{2} PRF. \tag{2.33}$$

The PRF of the radar system is chosen to detect targets up to an expected target velocity using (2.30), but the unambiguous range decreases as unambiguous velocity increases [2]. A radar system can be designed to transmit pulses at a staggered PRF, which means that the period between consecutive pulse transmissions is not consistent from one pulse to the next. A staggered PRF can raise the first blind velocity without reducing the unambiguous range to the extent that a constant PRF would be reduced [13]. As a result of a staggered PRF, clutter echoes no longer alias to all integer multiples of the PRF and targets with Doppler shifts near an integer multiple of the PRF are more likely to be detected. Surveillance radars are often designed to transmit pulses at a staggered PRF to increase target detection by reducing the impact of blind speeds, and ensure accurate target detection by reducing the likelihood of range and Doppler ambiguities.

To measure how a staggered PRF impacts a system's unambiguous range and blind velocities, a set of P staggered pulses are written as $\{PRF_P\} = \{PRF_0, PRF_1, ..., PRF_{P-1}\}$ [7]. PRF_P can be rewritten as a set of integer multiples of the greatest common divisor (gcd), f_g, as $PRF_P = k_P$ gcd $(PRF_0, PRF_1, ..., PRF_{P-1})$, or

$$PRF_P = k_P f_g, \tag{2.34}$$

where k_P is a set of values known as staggers, and the stagger ratio is the ratio between any two staggers in the set [7]. The first blind Doppler frequency f_{BS} for a staggered PRF system is the least common multiple (lcm) of the PRFs as $f_{BS} =$ lcm $(PRF_0, PRF_1, ...,$ $PRF_{P-1},)$, or

$$f_{BS} = f_g \text{ lcm } (k_0, k_1, ...k_{P-1}). \tag{2.35}$$

Suppose that there exists a radar system whose PRF (PRF_{US}) is constant and is the average value of PRF_P as

$$PRF_{US} = \frac{f_g}{P} \sum_{p=0}^{P-1} k_P. \tag{2.36}$$

The ratio f_{BS}/PRF_{US} is used to calculate how much a staggered PRF increases the first blind velocity of the system [7]. For example, the first blind velocity of a two-pulse stagger system with stagger ratio is 6:7 would be 6.46 times greater than the constant PRF system. The unambiguous range of a constant PRF system is c/2PRF, while a staggered PRF system's (R_{uas}) is determined by the largest PRF of PRF_P, or

$$R_{uas} = \frac{c}{2 \text{ max}(PRF_P)}. \tag{2.37}$$

The unambiguous range of a two-pulse stagger system with stagger ratio 6:7 is 92.86% of the constant PRF system. Doppler ambiguities or missed target detections due to blind speeds are generally more harmful to a surveillance radar than range ambiguities, so the unambiguous range is typically degraded to increase the first blind speed as presented in the previous example.

2.3 Radar Range Equation

Radar detection performance is heavily affected by the amount of energy reflected by the target to the surveillance radar system. A radar signal is susceptible to many losses while propagating, and the radar cross section (RCS) of a target controls how much energy will be reflected to the radar. The radar range equation is a helpful tool for calculating the expected received energy of a radio wave transmitted by the radar and reflected by a target, written as

$$P_r = \frac{P_t G_t G_r \lambda^2 \sigma}{(4\pi)^3 L_s L_a R^4} \tag{2.38}$$

where P_r is the received power (Watts), P_t is the transmitted power (Watts), G_t is the gain of the transmit antenna, G_r is the gain of the receive antenna, λ is the wavelength of the radio wave (meters), σ is the RCS of the reflecting object (square meters, or meters^2), L_s are system losses, L_a are atmospheric losses, and R is the range from the radar to the reflecting object (meters) [2]. Losses due to the system and atmosphere are ignored in this work and will be excluded in any references to the radar range equation.

Surveillance radar systems often employ directional antennas (as opposed to isotropic antennas) which focus the energy of a transmitted pulse to the boresight of the antenna [7]. The gain of a rectangular antenna aperture is related to its effective aperture, A_e, as

$$G = \frac{4\pi A_e}{\lambda^2} \tag{2.39}$$

where λ is the carrier wavelength of the transmitted radar signal [14]. The gain terms, G_t and G_r, can be combined into a single term, G^2, when the surveillance radar system shares the antenna for the transmit and receive subsystems. The antenna's one-way power pattern, $P(\theta, \phi)$, describes the radiated power as a function of angles azimuth, θ, and elevation, ϕ, relative to the antenna's boresight. The maximum value of $P(\theta, \phi)$ is achieved when θ and

ϕ are precisely the antenna's boresight. The one-way power pattern of an antenna is related to the radiated electric field intensity, $E(\theta, \phi)$ [7], as

$$P(\theta, \phi) = |E(\theta, \phi)|^2 \tag{2.40}$$

and the electric field intensity in azimuth is given by

$$E(\theta, \phi) = \text{sinc}\left(\left(\frac{D_y}{\lambda}\right)\ \text{sin}(\theta)\right)\ \text{sinc}\left(\left(\frac{D_z}{\lambda}\right)\ \text{sin}(\phi)\right) \tag{2.41}$$

where $\text{sinc}(x) = \frac{\sin(\pi x)}{\pi x}$, λ is the carrier wavelength of the transmitted radar signal, and D_y and D_z are the aperture size in the y and z dimensions. The one-way radiation power pattern for a rectangular aperture as a function of angles θ and ϕ has the form [15]

$$P(\theta, \phi) = \text{sinc}^{\,2}\left(\left(\frac{D_y}{\lambda}\right)\ \text{sin}(\theta)\right)\ \text{sinc}^{\,2}\left(\left(\frac{D_z}{\lambda}\right)\ \text{sin}(\phi)\right). \tag{2.42}$$

A surveillance radar scanning for targets near the Earth's surface will receive reflections from surface clutter, such as foliage, buildings, mountains, and ocean waves. Surface clutter is a distributed scatterer, which means that its RCS σ is defined over an area as [2]

$$\sigma = A\sigma^0 \tag{2.43}$$

where A is the surface area of the clutter and σ^0 is the scattering coefficient of the clutter with dependencies on its grazing angle, wavelength, polarization, and material. With inspiration from Richards [7], the geometry of a radar beam illuminating a flat surface with grazing angle δ is shown in Figure 2.10. The radar has a 3-dB beamwidth ϕ_3 and is positioned at a height H above the surface; the width of the main beam at range R_0 is approximately $R_0\phi_3$, and it is projected to $R\phi_3/\text{sin}(\delta)$ on the clutter surface. The range resolution, ΔR, of the radar signal is projected onto the clutter surface as $\Delta R/\cos(\delta)$, as shown in Figure 2.11.

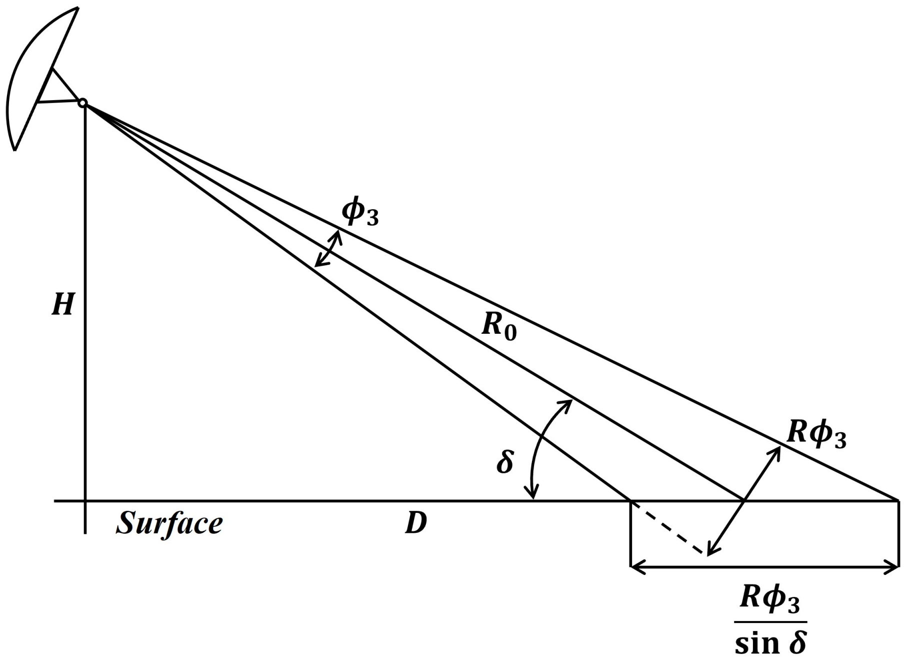

Figure 2.10: Surface illuminated by radar with elevation beamwidth ϕ_3

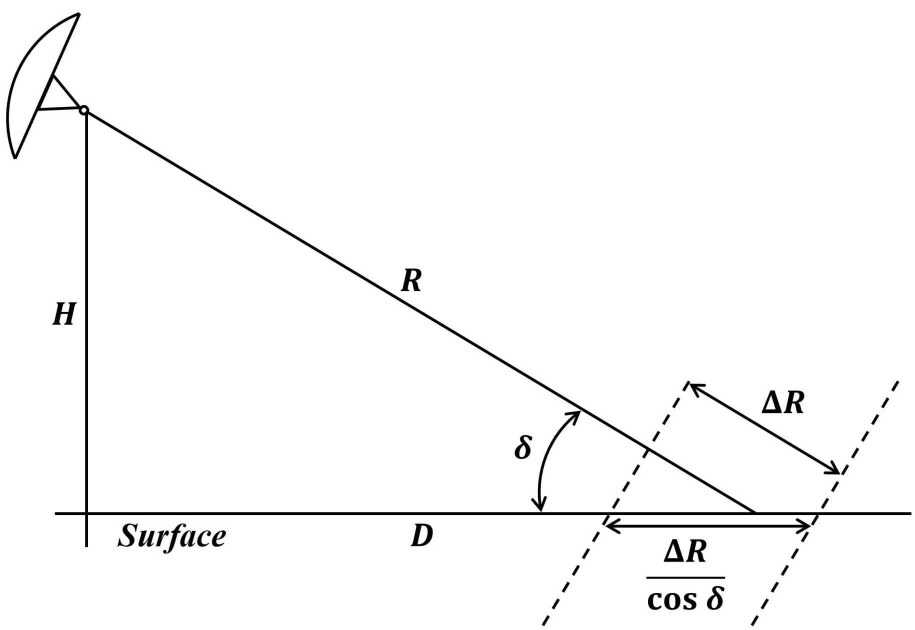

Figure 2.11: Projection of range resolution onto surface

To calculate the expected received energy from the clutter surface, two scenarios that depend on the radar's range resolution are considered. In the first scenario, the range resolution projected on the clutter surface is less than the projection of the main beam ($\Delta R/\cos(\delta) < R\phi_3/\sin(\delta)$), in which the resolution cell is resolution limited [7]. In the second scenario, the main beam projected on the clutter surface is less than the range resolution's projection ($\Delta R/\cos(\delta) > R\phi_3/\sin(\delta)$), in which the resolution cell is beam limited [7]. The differential RCS for each surface scatterer illuminated by the radar's beam is written related to its differential area as

$$d\sigma = \sigma^0(\delta)\ \delta_D(R - R_0)dA \tag{2.44}$$

where $\delta_D(\cdot)$ is the Dirac impulse function [7]. The radar range equation is expressed as an integral over the differential area as [7]

$$P_r(t_0) = \frac{P_t G^2 \sigma^0}{(4\pi)^3 R_0^4} \int_{\Delta A} P^2(\theta, \phi) dA. \tag{2.45}$$

When the illuminated surface clutter is beam limited, the differential surface area is

$$dA = \frac{R_0^2}{\sin\delta} d\theta d\phi. \tag{2.46}$$

The integral can be evaluated over the area contained by the 3-dB beamwidths of the main beam, and P_r reduces to

$$P_r(t_0) = \frac{P_t G^2 \lambda^2 \phi_3 \theta_3 \sigma^0}{(4\pi)^3 R_0^2 \sin\delta}. \tag{2.47}$$

In the resolution limited scenario, the differential surface area is

$$dA = \frac{R_0 \Delta R}{\cos\delta} d\theta, \tag{2.48}$$

and P_r reduces to

$$P_r(t_0) = \frac{P_t G^2 \lambda^2 \Delta R \theta_3 \sigma^0}{(4\pi)^3 R_0^3 \cos\delta}. \tag{2.49}$$

Each clutter scatterer on the Earth's surface has a unique grazing angle with respect to the surveillance radar. At very low grazing angles, a clutter scatterer appears "smooth" to the radar, and the incident energy from a radio wave will be reflected away from the radar [2]. As a result, little energy is reflected from a low-grazing angle scatterer back to the radar. Conversely, a clutter scatterer is likely to reflect most of the incident energy from a radio wave back to the radar at high grazing angles. The plateau region [4] is a term for the region of grazing angles between the low and high grazing angle regions. Scatterers whose grazing angle falls in the plateau region are considered "rough," and the intensity of their reflected energy can vary significantly.

A surface is considered smooth if the fluctuations to the surface height are relatively small. Rayleigh's criterion for smoothness is

$$\sigma < \frac{\lambda}{8\sin(\delta)} \tag{2.50}$$

where σ is the standard deviation of the surface clutter's height, λ is the carrier wavelength, and δ is the grazing angle [4]. A reference work by Ulaby, Moore, and Fung [4] argued that the Fraunhofer criterion is more accurate for a surface to be termed "smooth," as opposed to the Rayleigh criterion. The Fraunhofer criterion requires

$$\sigma < \frac{\lambda}{32\sin(\delta)}, \tag{2.51}$$

which aligns more closely with experimental observations of "smooth" and "rough" surface clutter radar measurements [4]. Note that the Fraunhofer criterion depends on the carrier frequency of the radar signal; surveillance radars with carrier frequencies greater than 1

GHz scanning for targets in natural terrains (i.e., the Earth's surface) are not likely to meet this criterion.

A homogeneous clutter surface model, or a surface composed of randomly distributed scatters with approximately the same RCS, results in a received signal whose square magnitude is exponentially distributed [2]. The Earth's surface is nonhomogeneous due to the variations in the materials it is composed of (sand, rock, soil, foliage, water, etc.) and surface height (hills, valleys, and mountains). The RCS for nonhomogeneous rough surfaces, such as the Earth's surface, tends to follow "heavy-tailed" distributions, such as Weibull, K, or lognormal distributions [2]. These distributions are described as "heavy-tailed" because a scatterer with a large RCS value is more likely to occur than in the homogeneous clutter model, resulting in a greater likelihood of large-amplitude echoes in the received signal. When the received signal contains echoes from surface clutter whose RCS is described by a heavy-tailed distribution, the false alarm rate of the surveillance radar's detector is expected to increase.

2.4 Received Signal Model

The signal received by a surveillance radar can be written as the sum of interference and target echo signals as $y(t) = w(t) + s(t)$, where $y(t)$ is the received signal, $w(t)$ is the interference signal, and $s(t)$ is the target echo signal. The signal $w(t)$ is the sum of multiple sources of interference, such as clutter echoes $w_c(t)$, thermal noise $w_n(t)$, and electromagnetic interference $w_i(t)$, which can be written as $w(t) = w_c(t) + w_i(t) + w_n(t)$. The following subsections derive models for each interference source and target echo signals.

2.4.1 Targets and Surface Clutter

Suppose that a mechanically steered surveillance radar is rotating in azimuth and transmitting radar signals to scan for targets. The target echo signal received after the p^{th} pulse is transmitted is written as

$$s(t;\theta_p) = \alpha_t(\tau,\theta,\phi;\theta_p)\ \tilde{x}(t-\tau)\ \text{exp}\ (j2\pi f_D t) \tag{2.52}$$

where $\tau = 2R/c$, θ and ϕ are the azimuth and elevation angles between the target and the boresight of the antenna at the time of pulse transmission, exp $(j2\pi f_D t)$ is a Doppler frequency shift of the wave echo due to relative motion between the target and the radar, $x(t)$ is the transmitted radar signal, and $\alpha_t(\tau,\theta,\phi)$ is derived from the radar range equation as

$$\alpha_t(\tau,\theta,\phi;\theta_p) = \sqrt{\frac{P_t G^2 \lambda^2 \sigma}{(4\pi)^3 R^4} P^2(\theta,\phi)}. \tag{2.53}$$

The surface clutter signal resembles a target echo signal, but differs as it is the sum of the reflections from each scatterer on the clutter surface as

$$w_c(t;\theta_p) = \int \int_{\Delta A} \alpha(\tau,\theta,\phi;\theta_p)\ \tilde{x}(t-\tau)\ \text{exp}\ (j2\pi f_D t) dA d\tau. \tag{2.54}$$

In Section 2.3, two cases were considered to determine the expected received energy from surface clutter. For the beam limited scenario, the received clutter signal after the p^{th} pulse transmission is given by

$$w_c(t;\theta_p) = \int \int \int \alpha(\tau,\theta,\phi;\theta_p)\ \tilde{x}(t-\tau)\ \text{exp}\ (j2\pi f_D t) d\theta d\phi d\tau, \tag{2.55}$$

where $\alpha_c(\tau, \theta, \phi)$ for each differential surface scatterer is

$$\alpha_c(\tau, \theta, \phi; \theta_p) = \sqrt{\frac{P_t G^2 \lambda^2 \sigma^0}{(4\pi)^3 R^2 \sin(\delta)} P^2(\theta, \phi)}. \tag{2.56}$$

In the resolution limited scenario, the clutter echo signal received after the p^{th} pulse transmission is given by

$$w_c(t; \theta_p) = \int \int \alpha(\tau, \theta, \phi; \theta_p)\, \tilde{x}(t - \tau) \exp(j2\pi f_D t) d\theta d\tau, \tag{2.57}$$

where $\alpha_c(\tau, \theta, \phi)$ for each differential surface scatterer is

$$\alpha_c(\tau, \theta, \phi; \theta_p) = \sqrt{\frac{P_t G^2 \lambda^2 \sigma^0 \Delta R}{(4\pi)^3 R^3 \cos(\delta)} P^2(\theta, \phi)}. \tag{2.58}$$

2.4.2 Thermal Noise

The thermal motion of electrons within a radar's receiver produce thermal noise [16], which is a zero-mean complex Gaussian random process that combines with electromagnetic interference, target echo, and clutter echo signals in the received signal. The power spectral density (PSD) of thermal noise, $S_n(F)$, is approximately

$$S_n(F) = kT \tag{2.59}$$

when $hF/kT << 1$; h is Planck's constant (6.6254×10^-34 Joules/second), F is in Hz, $S_n(f)$ is in Watts/Hz, k is Boltzmann's constant (1.38×10^{-23} Joules/Kelvin), and T is the absolute temperature of the noise source (Kelvins) [7]. The above definition implies that thermal noise has infinite power, which is not physically possible. Thermal noise has finite power, as (2.59) is an approximation that is valid for radio frequency systems with absolute temperatures greater than 50 Kelvins, and the bandwidth of the radar's receiver limits the spectrum of thermal noise in the received signal to $-\frac{B}{2} \leq F \leq \frac{B}{2}$ where B is the bandwidth in Hz [7].

The average noise power at the output of a system with transfer function $H(F)$ is found by

$$P_n = \int_{-\infty}^{\infty} S_n(F)|H(F)|^2 dF. \tag{2.60}$$

Assuming that the transfer function is ideal, the system is bandlimited to B Hz, and the absolute temperature of the noise is the standard temperature ($T = T_0 = 290$ Kelvins), the above reduces to

$$P_n = kT_0BG \tag{2.61}$$

where G is the gain of the system [7]. System losses introduced by non-ideal components in the receiver's hardware add noise power to the output of the receiver. The additional noise power due to system losses is written as

$$P_{sys} = kT_eBG, \tag{2.62}$$

where T_e is the effective temperature of the system in Kelvins [7]. The total noise power at the output of the receiver is thus

$$P_{tot} = P_n + P_{sys} = kT_0BG + kT_eBG. \tag{2.63}$$

A system's noise figure is a measure of the noise power introduced by system losses and the thermal noise at the input to the system, which is written as

$$F = \frac{P_{tot}}{P_n} = \frac{kT_0BG + kT_eBG}{kT_0BG}. \tag{2.64}$$

Ideally, a radar should be designed to have minimal system losses, but typical radar systems have noise figures between 2 and 10 dB [7].

2.4.3 Electromagnetic Interference

External sources of EM waves, such as power lines, cellular phones, and other radar systems, can contaminate the received signal and decrease the detectability of targets. In some cases, another system may radiate in the surveillance radar system's frequency band to intentionally degrade signal detection, known as jamming [7]. The abundance of wireless technologies in the modern era have congested the frequency spectrum and surveillance radars must be designed with these external sources in mind. The signal produced by electromagnetic interference sources is represented by $w_i(t)$ within this work. Although electromagnetic interference is non-zero in real radar systems, the process $w_i(t) = 0$ within the simulation as it is intentionally excluded. This work aims to investigate the impact of surface clutter on CFAR detector performance – the simulation and modeling of electromagnetic interference would distract from the focus of the work, and thus further discussions of electromagnetic interference are omitted.

2.5 Signal Processing Chain

Surveillance radars must process the received signal to mitigate the effects of interference for the optimal detection of targets. Clutter filtering techniques, such as the N-pulse canceller, can be implemented in a radar system to prevent clutter echoes from dominating the received signal [2]. The dynamic range of the received signal can be large, as the signal may contain small amplitude target echoes from long-range targets or large amplitude echoes from nearby objects. A log-magnitude detector can be used at the output of the clutter filter to compress the dynamic range of the received signal onto a logarithmic scale [17]. The output of the log-magnitude detector, however, does not retain the phase information of the received signal. A processing interval of radar measurements must be summed non-coherently (unlike the coherent sum performed in pulse-Doppler processing) to achieve an integration gain and thereby increase the SNR of target echoes [2]. The following subsections describe the clutter filter, log magnitude detector, and non-coherent integrator implemented in an example processing chain to convert the received signal into test statistics, which can be used to identify targets in the received signal.

2.5.1 Clutter Filtering

Clutter echo signals closely resemble target echo signals, as they are both time-delayed and amplitude-scaled copies of the transmitted radar signal that may be Doppler shifted; however, surface clutter is mostly stationary while targets are generally non-stationary. The matched filter output of clutter echo signals will be relatively larger than non-stationary target echo signals due to their higher correlation to the signal in which the matched filter was designed. Additionally, signal processing chains typically implement a coherent or noncoherent integrator to improve the SNR of target echo signals but also unintentionally increase the interference power of clutter echoes. Clutter echoes can increase the false alarm rate of surveillance radars, and thus a clutter filter is a necessary step in the signal processing chain.

Consider a stationary radar system that illuminates stationary surface clutter with pulses of radar signals. The amplitude and phase of the wave echo received by the clutter scatterer should be the same for each slow-time radar measurement (ignoring the effects of thermal noise), and thus subtracting a set of radar measurements from another set across the slow-time dimension should cancel clutter echo signals for each range bin [2]. The two-pulse canceller is a simple clutter filter design which "cancels" clutter echoes by subtracting radar measurements from the same range bin over a pair of successive pulses [2]. The amplitude and phase of non-stationary target echo signals change across slow-time radar measurements, so the energy of target echo signals is expected to be maintained at the output of the clutter canceller.

The frequency response of clutter filters generally resemble high-pass filters with a null near zero Doppler frequency, as they are designed to reduce the impact of stationary clutter and maintain the amplitude of target echoes [2]. The two-pulse canceller is modeled as $z[m] = y[m] - y[m-1]$, where $z[m]$ is the filter output and $y[m]$ is the input at index m. The discrete-time transfer function of the two-pulse canceller is given by $H(z) = 1 - z^{-1}$, with filter coefficients [1 -1], and thus the Doppler frequency response is given by [2]

$$\begin{aligned} H(f_D) &= (1 - z^{-1})|_{z=\exp(j2\pi f_D T)} = 1 - \exp(-j2\pi f_D T) \\ &= \exp(-j\pi f_D T)(\exp(j\pi f_D T) - \exp(-j\pi f_D T)) \\ &= 2j\exp(-j\pi f_D T)\sin(\pi f_d T), \end{aligned} \tag{2.65}$$

where T = 1/PRF. The magnitude of a two-pulse canceller's frequency response can be seen in Figure 2.12a where the PRF = 1 kHz. Even though f_D only ranges from -PRF/2 to PRF/2 in the figure, the frequency response is periodic and the null at zero Doppler frequency occurs at integer multiples of the PRF for a constant PRF radar system.

The two-pulse canceller can be extended to an N-pulse canceller to achieve a higher-ordered filter response [2]. The simplest approach to design an N-pulse canceller is achieved by cascading $N-1$ two-pulse cancellers. The transfer function of the N-pulse canceller composed of cascaded two-pulse cancellers has the form

$$H_N(z) = (1 - z)^{N-1}. \tag{2.66}$$

The frequency response of an example cascaded N-pulse canceller is shown in Figure

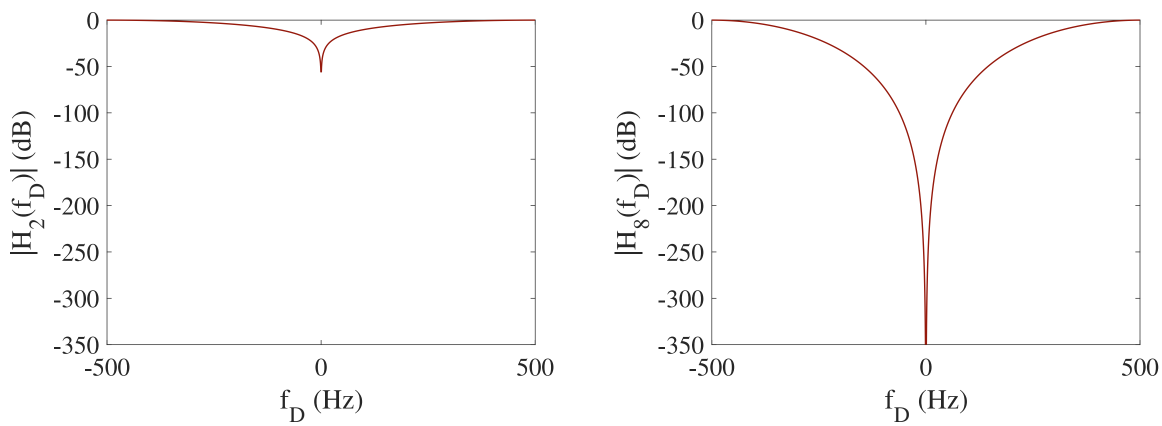

(a) Two-Pulse Canceller (b) Eight-Pulse Canceller

Figure 2.12: Normalized frequency responses of the two- and eight-pulse cancellers

2.12b. The value of N for this example was 8, and the filter response featured a much wider and deeper null centered at zero Doppler frequency when compared to the two-pulse canceller. The higher-order filter would likely perform better for clutter cancellation in a real radar system, as clutter is not perfectly stationary and may Doppler shift the radar signal echo, but the computational load of the filter increases as N increases [2].

An alternative approach to designing the N-pulse canceller involves adjusting the filter coefficients of the clutter filter. The filter coefficients of the eight-pulse canceller in the previous example can be found by expanding (2.66) to

$$\begin{aligned} H(f_D) &= (1 - z^{-1})^7 \\ &= 1 - 7z^{-1} + 21z^{-2} - 35z^{-3} + 35z^{-4} - 21z^{-5} + 7z^{-6} - z^{-7}, \end{aligned} \tag{2.67}$$

and thus the filter coefficients are [1 -7 21 -35 35 -21 7 -1]. The values for the filter coefficients can be adjusted to achieve a desired frequency response, but the sum of the filter coefficients generally evaluates to zero in order to cancel zero Doppler clutter [2].

The frequency response of discrete time filters are periodic for constant PRF systems, and the zero Doppler null of the clutter filter repeat at integer multiples of the PRF. These repetitive nulls create blind zones in the received signal [2], where the energy of target echoes from targets with Doppler frequencies near integer multiples of the PRF will be attenuated by the clutter filter, and the targets would likely not be detected by the radar. In Section 2.2, the idea of radar systems transmitting pulses at a staggered PRF to combat blind speeds was presented. The squared magnitude of the average frequency response from the two-pulse canceller with a staggered PRF input is written as [7]

$$|H_{2,P}(f)|^2 = \frac{4}{P}\sum_{p=0}^{P-1} \sin^2(\pi f/PRF_p). \tag{2.68}$$

Consider a radar system transmitting pulses at staggered intervals with a stagger ratio of 3:5 whose average PRF is 1 kHz. The first blind speed occurs at a Doppler frequency of 3.75 kHz, which is 3.75 times higher than a constant PRF system whose first blind speed occurs at a Doppler frequency corresponding to its PRF of 1 kHz. The frequency responses of the constant PRF and staggered PRF systems are shown in Figure 2.13. The frequency response of the two-pulse canceller for the staggered PRF system still features nulls, but they are not as frequent as the constant PRF system in the Doppler spectrum and only extend to ≈ -10 dB in this example.

2.5.2 Dynamic Range Compression

A surveillance radar converts the received signal into radar measurements by a process known as sampling, which involves the quantization of the analog received signal [2]. The ADC of the radar system samples the amplitude of the received signal and assigns a binary value with a finite number of bits (based on the ADC's resolution) to the measurement. The ADC maps the amplitude of the received signal to a discrete level from within its hardware; the levels are evenly spaced with a quantization step size Δ in uniformly-quantized ADCs [2]. A radar's ADC is capable of measuring the amplitude of the received signal up to the

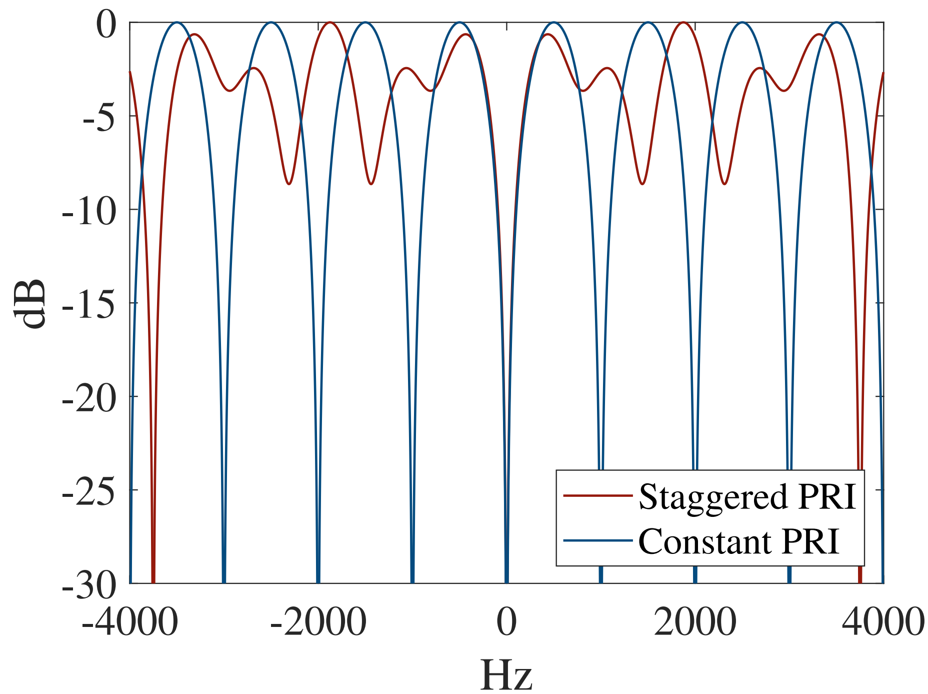

Figure 2.13: Squared magnitude of system frequency responses for constant and staggered PRI systems

maximum quantization level, and the dynamic range of the ADC is the ratio of the largest quantization level to the first quantization level. Suppose that the dynamic range of a radar system's ADC is large and uniformly quantized; it is possible that a small-amplitude target echo signal embedded in interference would not reach the next quantization level to be distinguished from interference, resulting in a target miss. The system would be considered saturated, as it has insufficient quantization levels for its wide dynamic range [2].

Analysis of the radar range equation shows that the energy of wave echoes from a target with a fixed RCS strongly depends on the range of the target. Suppose that the range of a target is doubled; the expected power received by the radar will decrease by a factor of 16 due to the R^4 term in the denominator of the radar range equation. Therefore, long range surveillance radars receive a signal that spans a wide dynamic range of echo powers (the ratio of a target echo's magnitude to receiver noise power) due to the range dependence of the energy of a wave echo, and a uniformly-quantized ADC measuring the amplitude of the received signal would likely be saturated. A surveillance radar may compress the dynamic range of the received signal by implementing a logarithmic amplifier to de-emphasize large amplitude echoes. A logarithmic amplifier converts an echo amplitude (A) to a log-magnitude value by [17]

$$\text{Log-magnitude (dB)} = 10\,\log_{10}[A^2]. \tag{2.69}$$

Doviak and Zrnic [17] provide an example range profile from a real radar system in which the received signal contains receiver noise (10^{-14} W) and echoes from nearby ground clutter, TV towers, and atmospheric phenomena. They state that the echo power (A^2) of the strongest echo in the received signal was 10^9 more intense than the receiver noise, which corresponds to a dynamic range of 90 dB. Legacy radar systems have a limited dynamic range on their display, and a logarithmic amplifier allows for large amplitude echoes from nearby targets to be shown on the same display as small amplitude echoes from long range targets [17]. The measurement of fluctuations in atmospheric phenomena would likely not be possible for their radar system without the logarithmic amplifier, and strongest echo from their example would likely saturate the display.

2.5.3 Noncoherent Integration

A CPI of uniformly-spaced radar measurements can be processed into a range-Doppler map via the FFT or DFT, which increases the SNR of target echo signals due to integration gain [2]. Suppose that a radar receives a signal, $y(t)$, that is composed of thermal noise, $w_n(t)$, and target echo signals, $s(t)$, as $y(t) = w(t) + s(t)$, and thus its radar measurements can be written as $y[m] = s[m] + w[m]$. Also suppose that a target in the received signal is moving at a constant velocity towards the radar, its RCS is constant over the CPI, its target echo signal resolves to a single range bin over the CPI (i.e. $s[m]$ = constant = A exp$[j\phi]$) [2]. The integration of M slow-time radar measurements from the target's range bin (y_M) is [2]

$$\begin{aligned} y_M &= \sum_{m=0}^{M-1}(s[m] + w[m]) = \sum_{m=0}^{M-1}(A\,\text{exp}[j\phi] + w[m]) \\ &= MA\,\text{exp}[j\phi] + \sum_{m=0}^{M-1} w[m]. \end{aligned} \tag{2.70}$$

The signal power of the target echo signal therefore increases by M^2A^2, while the thermal noise power (σ_n^2) increases by [2]

$$\begin{aligned} E\left\{\left|\sum_{m=0}^{M-1} w_n[m]\right|^2\right\} &= E\left\{\left(\sum_{m=0}^{M-1} w_n[m]\right)\left(\sum_{l=0}^{M-1} w_n^*[l]\right)\right\} \\ &= \sum_{m=0}^{M-1}\sum_{l=0}^{M-1} E\{w_n[m]w_n^*[l]\} \\ &= M\sigma_n^2. \end{aligned} \tag{2.71}$$

The SNR of the target echo signal before integration is A^2/σ_n^2, and its SNR increases to by a factor of M to $M^2A^2/M\sigma_n^2$, or MA^2/σ_n^2 after integration [2]. A radar system may transmit pulses at staggered intervals to reduce the impact of blind zones or range and Doppler ambiguities in the received signal, however, the system cannot create a range-Doppler map via the FFT due to the non-uniform spacing of slow-time radar measurements. Range-Doppler maps can still be generated from radar measurements by adjusting the definition of the DFT to account for the non-uniform intervals between pulses [5], but at an increased computational load due to the increase in complexity from the FFT to the DFT. Legacy radar systems often do not have the hardware and computational power required to implement such DFT algorithms, and thus it is not feasible for computationally-limited systems to coherently integrate non-uniformly spaced radar measurements.

Radar systems incapable of coherent integration may take the magnitude, log-magnitude, or squared magnitude of the received signal, which discards phase information, and then noncoherently sum across slow-time radar measurements to increase the SNR target echo signals. The noncoherent integration gain of target echo signals is not as easily quantifiable as given by (2.70) due to the magnitude, squared magnitude, and log-magnitude operations resulting in cross product terms of the target echo samples and thermal noise samples [2]. Previous works used Albershim's equation [2, 18] and found that the noncoherent integration of M slow-time radar measurements achieves an integration gain of nearly M for high-SNR targets and an integration gain of nearly $\sqrt{M}$ for low-SNR targets. The integration gain of a noncoherent sum operation is always expected to be less than the integration gain of a coherent sum operation due to the omitted phase information from the radar measurements, but integration is often necessary to detect low-SNR targets [2].

Chapter 3

Detection Theory

A surveillance radar system transmits pulses of radio waves and receives a signal that may contain echoes from targets. The received signal is corrupted by interference, namely thermal noise, electromagnetic interference, and clutter echoes, meaning that a target echo may not be easily distinguishable. Test statistics are scalar quantities sampled from the processed received signal that can indicate the presence of a target. Threshold detection is a method of target identification that involves the comparison of a test statistic with a threshold for deciding between two competing hypotheses. A test statistic less than the threshold is assumed to contain interference alone (the null hypothesis ($\mathcal{H}_0$)) while a test statistic greater than the threshold is assumed to contain interference and energy from a target echo (the alternative hypothesis ($\mathcal{H}_0$)) [19]. The hypotheses for a test statistic may be written as

$$\mathcal{H}_0 : y = w$$
$$\mathcal{H}_1 : y = w + s$$

where a random variable y represents the test statistic, which is composed of interference alone (w) under $\mathcal{H}_0$ or interference plus energy from a target echo ($w + s$) under $\mathcal{H}_1$ [2]. Once a test statistic is confirmed to contain energy from a target echo, its position can be estimated and passed to downstream radar systems, such as tracking.

The random variable y represents a test statistic and the random variables w and s are used to describe the hypotheses for a test statistic, which are different from the signals $y(t)$, $w(t)$, and $s(t)$ from the previous sections. Suppose that the received signal contains interference only, meaning no target echoes are present, and the interference signal was a zero-mean complex Gaussian random process. Assuming the processing applied to the received signal is square law, the probability density function (PDF) of y would be expected to follow an exponential distribution, as the squared magnitude of a zero-mean complex Gaussian random process is exponentially distributed [3]. Although $y(t)$ and y are not interchangeable, the PDF of y is related to the statistical behavior of $y(t)$. Similarly, w and s are not interchangeable with $w(t)$ and $s(t)$, but it follows that a test statistic composed of interference only ($y = w$) would correspond to the received signal containing interference only ($y(t) = w(t)$), while a test statistic containing interference and energy from a target echo would correspond to the received signal containing interference and a target echo signal ($y(t) = w(t) + s(t)$).

A graphical representation of threshold detection is provided in Figure 3.1, where a threshold of magnitude 6.5 is compared to a band of test statistics from contiguous range bins. All test statistics in this set are selected as the null hypothesis except at index 12, which is the alternative hypothesis. Threshold detection is susceptible to two types of errors. Type I errors occur when interference alone is greater than the threshold, otherwise known as a false alarm [2]. The target at index 12 may be a false alarm, which implies that the test statistic did not actually contain energy from a target echo and interference alone was greater than the threshold. The false alarm would then waste resources of downstream processors due to the non-existent target. A Type II error occurs when a test statistic contains energy from a target echo but falls below the threshold, also known as a target miss [2]. Target misses are undesirable for surveillance radar systems.

The threshold's magnitude controls the probability that Type I and II errors occur. Type I errors are associated with the probability of false alarm, P_{FA}, while Type II errors are

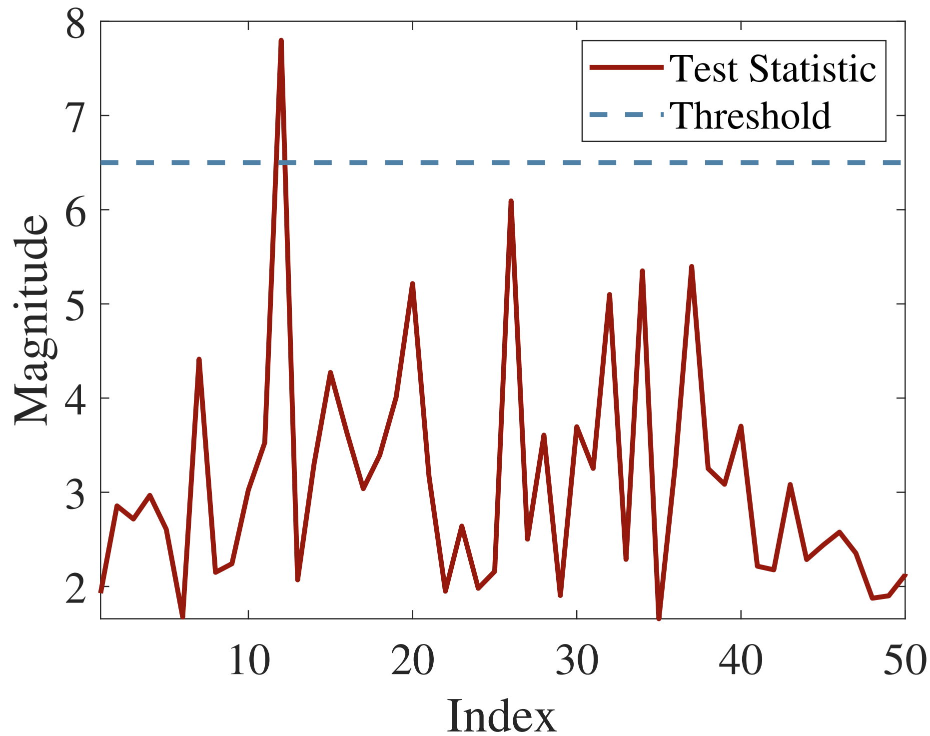

Figure 3.1: Threshold detection for a set of test statistics

associated with the probability of a miss, $1-P_D$, which is the complement of the probability of detection, P_D. The PDF of a null hypothesis test statistic is denoted as $p(y;\mathcal{H}_0)$, while the PDF of an alternate hypothesis test statistic is denoted as $p(y;\mathcal{H}_1)$. It is not possible to minimize the false alarm and target miss probabilities simultaneously by adjusting the magnitude of the threshold for threshold detection regardless of the target and interference PDFs [19]. As the threshold is increased, P_{FA} decreases and $1-P_D$ increases, and as the threshold is decreased, P_{FA} increases and $1-P_D$ decreases. Figure 3.2 graphically represents an example of the threshold, P_{FA}, and $1-P_D$ for $p(y;\mathcal{H}_0)$ and $p(y;\mathcal{H}_1)$.

The signal-to-interference-plus-noise ratio (SINR) is a quantity that measures the signal power received from the target echoes divided by the interference and noise power. As SINR increases, P_{FA} and $1-P_D$ can both decrease due to less overlap of the $p(y;\mathcal{H}_0)$ and $p(y;\mathcal{H}_1)$ curves. A target's signal power is related to its reflectivity, as seen in Section

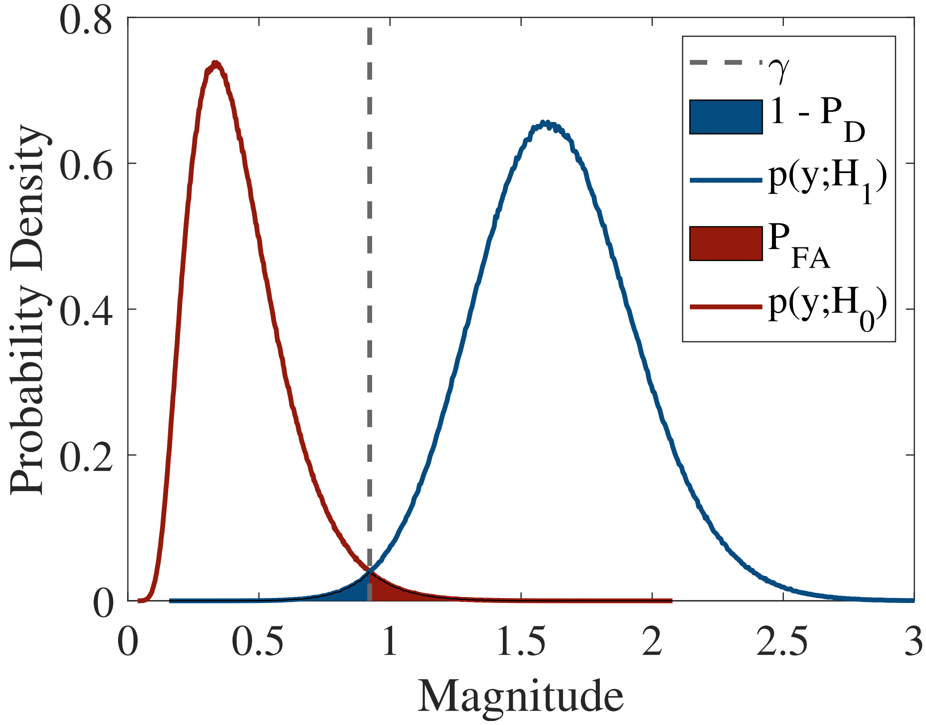

Figure 3.2: Test statistic distributions

2.3, and cannot be increased unless the target's range decreases or the surveillance radar's transmit power is increased. Filtering and other signal processing techniques are required to maintain signal power and reduce the interference power, as discussed in Section 2.5, which increases the SINR and P_D while lowering P_{FA} as desired.

False alarms are unavoidable due to the probabilistic nature of test statistics, but a low, constant P_{FA} may prevent downstream systems from being overwhelmed with detections. Additionally, radar detectors are typically designed to follow the Neyman-Pearson criterion, where target detection is maximized for a threshold that achieves a constant false alarm rate (CFAR) [19]. A constant threshold can be used for a set of independent and identically distributed (IID) test statistics when $p(y; \mathcal{H}_0)$ is known, and false alarms will be generated with a constant P_{FA}. Choosing a constant threshold for a set of test statistics when $p(y; \mathcal{H}_0)$ is unknown, or when $\mathcal{H}_0$ test statistics are non-IID, will produce false alarms at an unpredictable rate [3]. The threshold used by the radar's detector must estimate the interference statistics for a set of test statistics in order to stabilize the false alarm rate.

CFAR detectors adaptively calculate a threshold for each test statistic by assuming that the $\mathcal{H}_0$ test statistics follow some distribution, such as the exponential distribution, and calculate a local estimate of a statistical parameter for that distribution [2]. A CFAR detector's ability to adaptively set the threshold can combat non-stationary interference statistics (such as a local change in the mean value of interference), but its performance depends on the assumption that the distribution of $\mathcal{H}_0$ test statistics is known. The distribution for a set of test statistics are generally unknown, and the CFAR detector's assumption about the distribution can be incorrect. As the distribution for a set of test statistics deviates from the assumed exponential distribution, false alarms will be generated at an unpredictable and variable rate. A discussion of the design of CFAR detectors can be found in Section 3.2, and their performance on simulated nonhomogeneous test statistics is analyzed in Chapter 4 [2].

3.1 Likelihood Ratio Test

The Neyman-Pearson theorem concludes that the likelihood ratio test (LRT) is the most powerful test for assigning a hypothesis to a test statistic [19]. In other words, the probability of detection is maximized for a given probability of false alarm when the LRT is applied to the observed test statistic. The LRT is written as

$$\frac{p(y;\mathcal{H}_1)}{p(y;\mathcal{H}_0)} \underset{\mathcal{H}_0}{\overset{\mathcal{H}_1}{\gtrless}} \gamma \tag{3.1}$$

where the ratio of the target-plus-interference distribution to the interference-only distribution is known as the likelihood ratio, and y is a random variable that represents a test statistic, and γ is the threshold for the test statistic. The test is read as follows: if the likelihood ratio for an observed test statistic y is less than the threshold, y is chosen as the null hypothesis ($\mathcal{H}_0$), else it is chosen as the alternate hypothesis ($\mathcal{H}_1$) [2]. The LRT is an implementation of hypothesis testing that achieves optimal detection when the distributions $p(y;\mathcal{H}_0)$ and $p(y;\mathcal{H}_1)$ for a test statistic y are known [19].

Using the PDF of the interference-only test statistics, the probability of false alarm (P_{FA}) is found as

$$P_{FA} = \int_{\gamma}^{\infty} p(y;\mathcal{H}_0)dy \tag{3.2}$$

where γ, $p(y;\mathcal{H}_0)$, and P_{FA} are visually depicted in Figure 3.2. The relationship between P_{FA} and γ is defined by (3.2) when the PDF $p(y;\mathcal{H}_0)$ and its statistical parameters (such as mean and variance) are known. In many cases, the PDF $p(y;\mathcal{H}_0)$ and its statistical parameters are unknown and a model must be assumed for the interference test statistics to deduce a distribution for $p(y;\mathcal{H}_0)$. The statistical parameters of $p(y;\mathcal{H}_0)$ must then be estimated to determine a relationship between P_{FA}, γ, and $p(y;\mathcal{H}_0)$, as the statistical parameters are unknown and can change within a set of test statistics. The CFAR detectors in this work are designed to locally estimate the statistical parameters of $p(y;\mathcal{H}_0)$ to calculate a threshold for each test statistic to maintain a constant P_{FA} regardless of changes to the interference statistics.

3.2 CFAR Detectors

Test statistics compared to a constant threshold generate false alarms at a constant rate when the interference-only test statistics are IID. A set of test statistics may be nonhomogeneous, which means that parameters of the interference statistics change throughout the set, and comparing test statistics to a constant threshold results in an unpredictable P_{FA}. CFAR detectors are detection algorithms designed to produce a threshold that maintains a constant

P_{FA} from a local estimate of interference statistics. The subset of test statistics processed by the CFAR detector shown in Figure 3.3 are arranged in a one-dimensional CFAR window, but the CFAR window can be designed to include more dimensions if desired. One or more parameters of the interference statistics can be estimated from the training cells, or the test statistics positioned in the leading and lagging windows of the CFAR window. The interference statistics estimate is then multiplied by a CFAR constant to produce a threshold that is compared to the cell-under-test (CUT). After the CFAR window compares the threshold to the CUT, the CFAR window is shifted by one index over the subset of test statistics to calculate a threshold for the next CUT until all possible test statistics have been compared to thresholds.

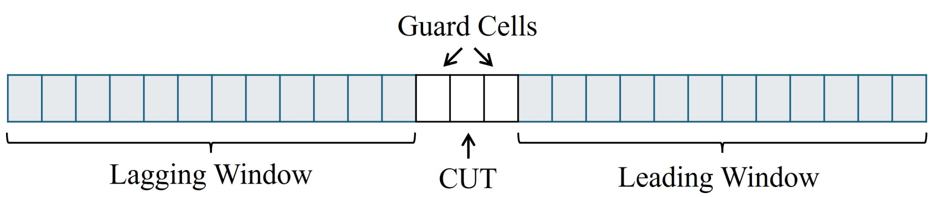

Figure 3.3: 1D CFAR window

Suppose that the in-phase and quadrature components of the interference signal received by a surveillance radar are normally distributed. The squared magnitude of a zero-mean complex Gaussian random variable is exponentially distributed [13], which means that the PDF of the interference-only test statistics will be distributed according to

$$p(y;\mathcal{H}_0) = \begin{cases} \frac{1}{\sigma_i^2} \exp\left[\frac{-y}{\sigma_i^2}\right], & y \geq 0 \\ 0, & y < 0 \end{cases} \tag{3.3}$$

where σ_i^2 is the expected value of the test statistics for a square law detector. The PDF of a target-plus-interference ($\mathcal{H}_1$) test statistic, assuming a Swerling 1 or 2 target model [13] is

$$p(y;\mathcal{H}_1) = \begin{cases} \frac{1}{\sigma_i^2+\sigma_t^2}\exp\left[\frac{-y}{\sigma_i^2+\sigma_t^2}\right], & y \geq 0 \\ 0, & y < 0 \end{cases} \tag{3.4}$$

where σ_t^2 is the variance of the target echo. The SINR is defined as σ_t^2/σ_i^2 for a Swerling 1 or 2 target in zero-mean complex Gaussian interference.

Substituting (3.3) into (3.2) and evaluating the integral yields the P_{FA} for exponentially distributed interference as

$$P_{FA} = \exp\left(\frac{-T}{\sigma_i^2}\right). \tag{3.5}$$

The threshold can be solved by applying a natural logarithm to both sides of the equation and some algebraic manipulation to produce

$$T = -\ln(P_{FA})\sigma_i^2 \tag{3.6}$$

which is the threshold for the Neyman-Pearson detector [2]. When σ_i^2 is unknown, a threshold T can be generated for the CUT of the CFAR window by estimating the interference power, $\hat{\sigma}_i^2$, and multiplying by a scale factor α derived from the exponential distribution and the desired P_{FA} as

$$T = \alpha\hat{\sigma}_i^2 \tag{3.7}$$

which resembles the threshold of (3.6). The scale factor α (referred to as a CFAR constant) for each CFAR detector will be presented in the following subsections.

3.2.1 CA-CFAR

A cell-averaging (CA) CFAR detector calculates a local estimate of the interference statistics based on the average value of the test statistics from the training cells in both the leading and lagging windows [20]. The noise power estimate $\hat{\sigma}_i^2$ is calculated as

$$\hat{\sigma}_i^2 = \frac{1}{N}\sum_{n=1}^{N} y_n \tag{3.8}$$

where y_n represents the n^{th} test statistic of the N training cells. The scale factor α_{CA} is found by

$$\alpha_{CA} = N[P_{FA}^{-1/N} - 1], \tag{3.9}$$

and the threshold for the CUT is thus [2]

$$T_{CA} = \alpha_{CA}\hat{\sigma}_i^2. \tag{3.10}$$

Note that the $1/N$ term from (3.8) and N term from (3.9) evaluate to unity in (3.10).

CA detectors perform best when the parameters of test statistics in the CFAR window are homogeneous and exponentially-distributed; the local estimate of the interference statistics can accurately represent the statistics of the cells in the window, and the threshold calculated for the CUT will achieve the desired P_{FA}. Situations can arise within the set of test statistics that bias the CA window's local estimate of interference statistics; in particular, clutter boundaries and target masking scenarios will be discussed. A clutter boundary is an abrupt change to the interference statistics within a window of test statistics [2]. Suppose that a subset of exponentially distributed test statistics with the same mean value are adjacent to another subset of exponentially distributed test statistics with a different mean value, as shown in Figure 3.4a. While the CFAR window contains only the first subset, the mean value of the first subset will be estimated by the CFAR detector and its threshold will be calculated accordingly. The CFAR window will then shift over the clutter boundary and its interference estimate will adjust as the test statistics from the second subset enter the CFAR window. One or more false alarms could be generated due to the biased interference statistics estimate, which are undesirable.

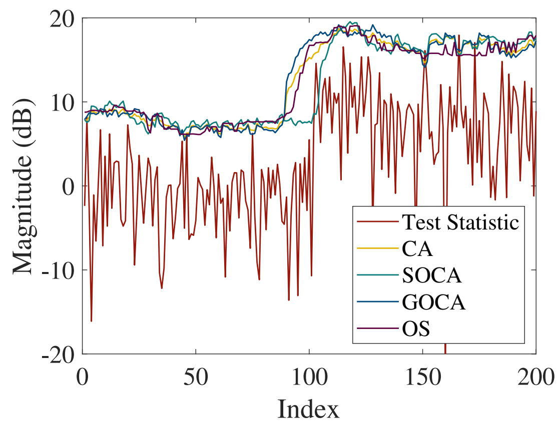

(a) Clutter Boundary

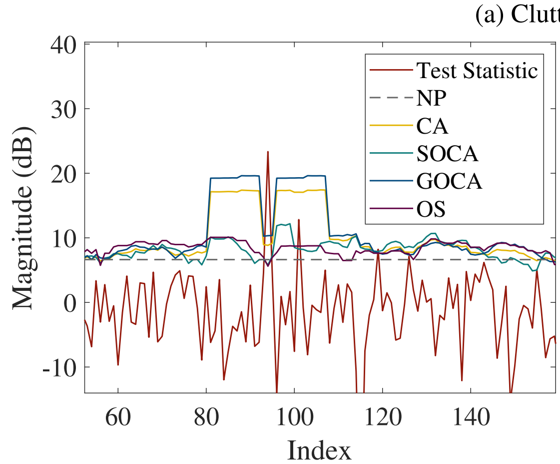

(b) Closely-Spaced Targets

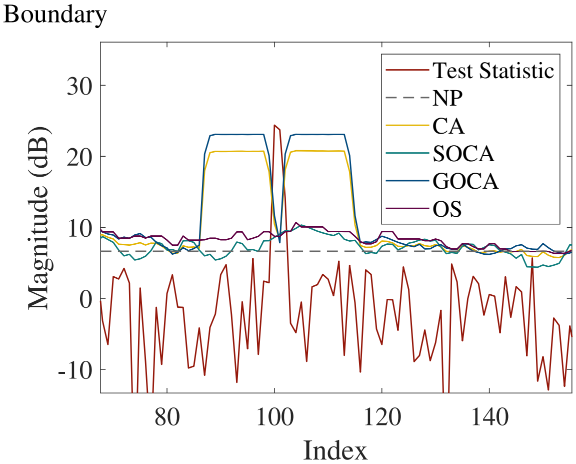

(c) Distributed Target

Figure 3.4: Clutter boundary and target masking scenarios, N_r = 12, N_g = 1

Target masking occurs when test statistics containing energy from target echoes are present in the leading or lagging window while the CUT contains a target echo [2]. Suppose that two or more targets are closely spaced in range and their target echoes are manifested in the test statistics of a given CFAR window, such as the targets in Figure 3.4b.

As the CFAR detector processes the test statistics, the interference statistic may be biased such that a test statistic is incorrectly hypothesized, meaning the target is assigned the null hypothesis because the threshold is greater than the magnitude of the test statistic. The detector would then incorrectly report the true number of targets and, in some extreme cases, all targets would be missed [2]. A distributed target is a special case of target masking where a target's echo is present in two or more consecutive test statistic cells, such as the target in Figure 3.4c [2]. The CFAR window is designed with one or more guard cells surrounding the CUT to reduce the impact of a distributed target or closely spaced targets biasing the threshold. Clutter boundaries and target masking degrade the local estimate of the interference statistics; variations of the CA detector have been designed to reduce the impact of these situations on the interference statistics estimate.

3.2.2 SOCA-CFAR

A "smallest-of" CA (SOCA) CFAR detector calculates a local estimate of the interference statistics by determining the average value of the leading and lagging windows separately, then choosing the smaller average [21]. The noise power estimated by a SOCA detector is calculated as

$$\hat{\sigma}_i^2 = \min(\hat{f}_{SO,lag}, \hat{f}_{SO,lead}) \tag{3.11}$$

where

$$\hat{f}_{SO,lag} = \sum_{n=1}^{N_r} y_n \tag{3.12}$$

$$\hat{f}_{SO,lead} = \sum_{n=N_r+1}^{N} y_n \tag{3.13}$$

and the scale factor is found iteratively from

$$P_{FA_{SO}} = 2[2+\alpha_{SO}]^{-N_r} \sum_{k=0}^{N_r-1} \binom{N_r-1+k}{k} [2+\alpha_{SO}]^{-k} \tag{3.14}$$

to produce a threshold for the CUT as [2]

$$T_{SO} = \hat{\sigma}_i^2 \alpha_{SO} \tag{3.15}$$

The SOCA detector was designed to reduce the impact of target masking by estimating the interference statistics of the smaller window. The detection performance of the SOCA detector is improved compared to the CA detector when one or more targets exist in the leading or lagging windows; however, the SOCA detector performs similarly to the CA detector when targets are present in both the leading and lagging windows. Note that N_r is the number of test statistics in the leading or lagging windows, which means that the sample size used to estimate the interference statistics is half that of the CA detector. The SOCA detector is expected to perform worse than the CA detector on a set of homogeneous test statistics, as the interference statistics estimate omits information from the test statistics in the larger window. Additionally, the SOCA detector is more prone to false alarms at clutter boundaries than the CA detector.

3.2.3 GOCA-CFAR

A "greatest-of" CA (GOCA) CFAR detector calculates a local estimate of the interference statistics by determining the average value of the leading and lagging windows separately, then choosing the larger average [22]. The noise power estimated by a GOCA detector is calculated as

$$\hat{\sigma}_i^2 = \max(\hat{f}_{GO,lag}, \hat{f}_{GO,lead}) \tag{3.16}$$

where

$$\hat{f}_{GO,lag} = \sum_{n=1}^{N_r} y_n \tag{3.17}$$

$$\hat{f}_{GO,lead} = \sum_{n=N_r+1}^{N} y_n \tag{3.18}$$

and the scale factor is calculated iteratively from

$$P_{FA_{GO}} = 2\left[[1+\alpha_{GO}]^{-N_r} - [2+\alpha_{GO}]^{-N_r}\sum_{k=0}^{N_r-1}\binom{N_r-1+k}{k}[2+\alpha_{GO}]^{-k}\right] \tag{3.19}$$

to produce a threshold for the CUT as [2]

$$T_{GO} = \hat{\sigma}_i^2\alpha_{GO} \tag{3.20}$$

The GOCA detector, like the SOCA detector, is reduced to N_r training cells for its interference statistics estimate. The GOCA detector combats false alarms generated by clutter boundaries, but its detection performance is generally degraded. Additionally, the risk of target misses due to target masking scenarios are worsened by the GOCA detector compared to the CA and SOCA detectors. A CFAR detector that reduces false alarms at clutter boundaries and increases target detection in target masking situations is desired, as the SOCA and GOCA CFAR detectors are not designed to perform well in both situations simultaneously.

3.2.4 OS-CFAR

An ordered-statistics (OS) CFAR detector calculates a local estimate of interference statistics by ranking the N test statistics within the leading and lagging windows, then choosing the k^{th} test statistic from the sorted set [23, 24]. The scale factor for a desired

P_{FA} is calculated using

$$P_{FA_{OS}} = k \binom{N}{k} \frac{(k-1)!(\alpha_{OS} + N - k)!}{(\alpha_{OS} + N)!} \tag{3.21}$$

and the threshold is thus

$$T_{OS} = \hat{\sigma}_i^2 \alpha_{OS} \tag{3.22}$$

where $\hat{\sigma}_i^2$ is the k^{th} test statistic of N sorted training cells. The OS detector combats clutter boundary and target masking scenarios, but is highly dependent on the k^{th} cell representing a good interference estimate for the set of test statistics. The value of k is typically chosen as $\frac{3}{4}N$, which removes $\frac{1}{4}N$ of the highest-ranking test statistics to calculate the interference statistics [2]. In general, the highest-ranking test statistics are assumed to be statistical outliers of interference test statistics, target echoes, or clutter boundaries. The design of the OS detector is advantageous because it is able to counteract said statistical outliers regardless of their position in the CFAR window; the performance of the SOCA and GOCA detectors are dependent on the clutter boundaries and target masking test statistics being contained in the leading or lagging windows.

3.3 Detector Performance

An example clutter boundary is shown in Figure 3.4a where the thresholds for each detector overlay the test statistics, and the CFAR constants of each detector were designed to achieve a P_{FA} of 0.01. The 200 test statistics are exponentially distributed; the first 100 are IID with a mean value of 1, and the second 100 are IID with a mean value of 10. In Figure 3.4a, the GOCA detector avoids a false alarm at the clutter boundary while the SOCA detector reports at least one detection. The thresholds from the OS and CA detectors are between the thresholds of the GOCA and SOCA detectors; in this example, the CA and

OS detector do not report detections at the clutter boundary.

A couple target masking examples are shown in Figures 3.4b and 3.4c. Each example are from a simulation of 200 exponentially distributed test statistics and the CFAR constants of each detector were designed to achieve a P_{FA} of 0.01. In Figure 3.4b, two exponentially distributed targets were simulated with mean value 100, and the remaining 198 test statistics have a mean value of 1. The SINR for this simulation was 100, or 20 dB. The index of each target was set such that one target would be in the leading or lagging window while the other was in the CUT of the CFAR window. As a result, the target at index 98 was correctly hypothesized by all detectors. The weaker target at index 101, however, was missed by the CA and GOCA detectors. In Figure 3.4c, a target with 20 dB SINR was simulated to span the test statistics from indices 99 to 101. The target was correctly identified by all detectors, which highlights the importance of guard cells for the CFAR detectors. In these target masking examples, the SOCA and OS detectors have improved detection performance than the CA and GOCA detectors. The OS detector outperforms the other CFAR detectors considering that it can detect closely-spaced targets and avoid false alarms at clutter boundaries.

A Monte Carlo simulation was conducted to investigate the performance of each detector on homogeneous, exponentially-distributed interference test statistics in the CFAR window. The mean value of these cells were set to 1, and the mean value of an exponentially-distributed target in the CUT was varied from 1 to 100. Figure 3.5 shows the observed probability of detection as a function of SINR, which is σ_t^2/σ_i^2 for this simulation. The NP detector achieves the highest P_D as it is the optimal detector when the distribution of the interference is known. The CA-CFAR detector performs second best, which is the expected result as the interference is homogeneous and exponentially-distributed. The SOCA, GOCA, and OS detectors perform slightly worse than the CA detector as they are designed for improved performance for target masking and clutter boundary scenarios, but they perform similarly to the CA and NP detectors.

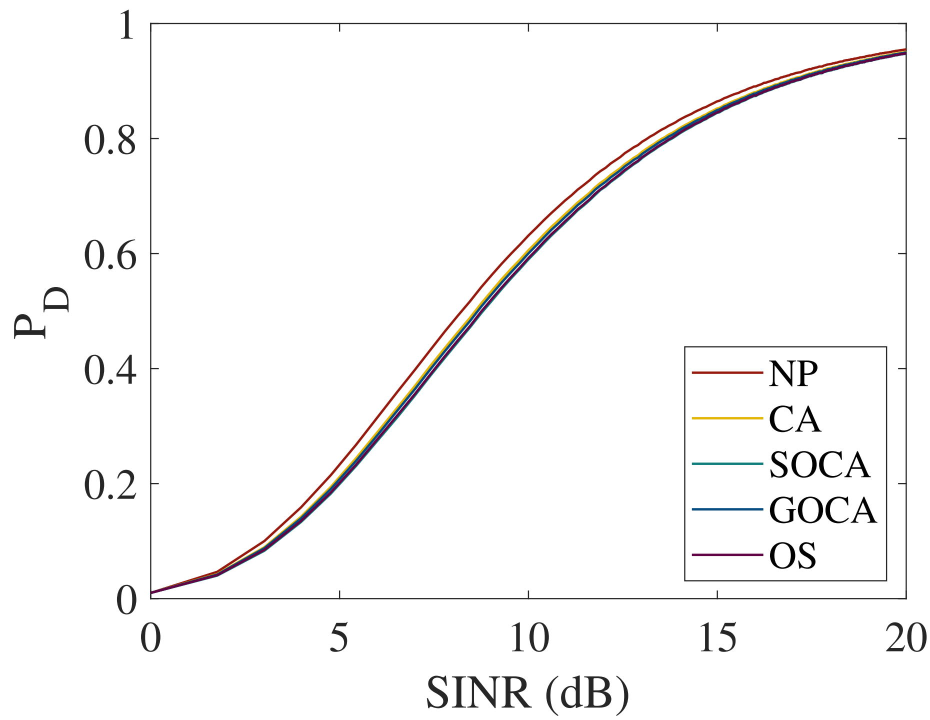

Figure 3.5: Exponentially distributed training cells, N_r = 12, P_{FA} = 0.01

Additional Monte Carlo simulations were conducted to investigate the detection performance for each detector in clutter boundary and target masking scenarios. In Figures 3.6a, 3.6b, and 3.6c, P_D as a function of SINR is shown for trials where the interference in the training cells were simulated with a mean value of 1, and clutter boundary cells in the leading window were simulated with a mean value of 10. The mean value of the simulated target cell in the CUT was then varied from 1 to 100 for each scenario. The clutter boundary degrades the P_D for the CA and GOCA detectors, which is due to the increased interference statistic estimate from the biased cells in the CFAR window. As the number of clutter boundary cells is increased in the leading window, the P_D for each CFAR detector is degraded except for SOCA because only the leading window was simulated to contain the clutter boundary. The interference statistic estimate for the OS detector was chosen as the 75^{th} percentile, or the 18^{th} cell of 24 cells in the training window, and its performance degrades as the number of clutter boundary cells increased, but its performance did not degrade to the extent of the CA and GOCA detectors. The OS detector was designed to omit the largest 6 cells in the CFAR window for this simulation; it is likely that the 18^{th} test statistic for the trials from Figure 3.6c was from the clutter boundary which explains its degraded detection performance.

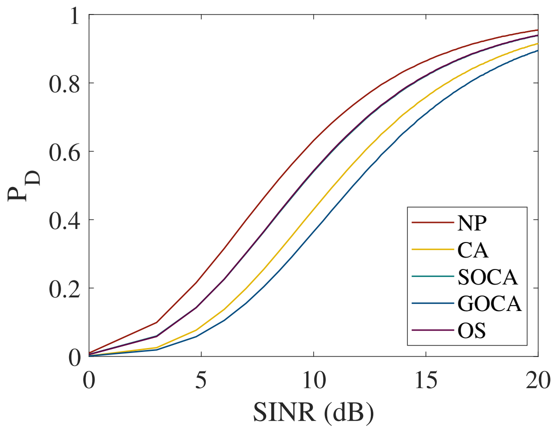

(a) 2 Cells in Leading Window

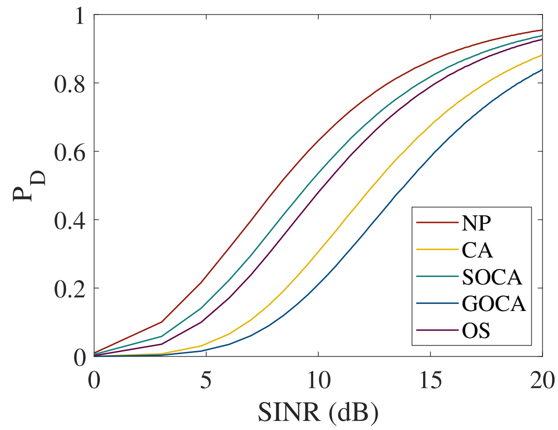

(b) 4 Cells in Leading Window

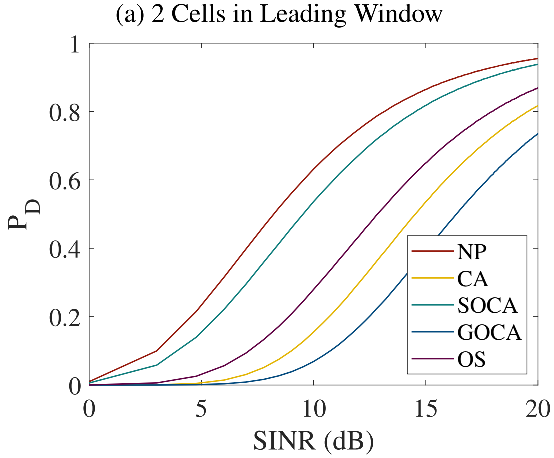

(c) 8 Cells in Leading Window

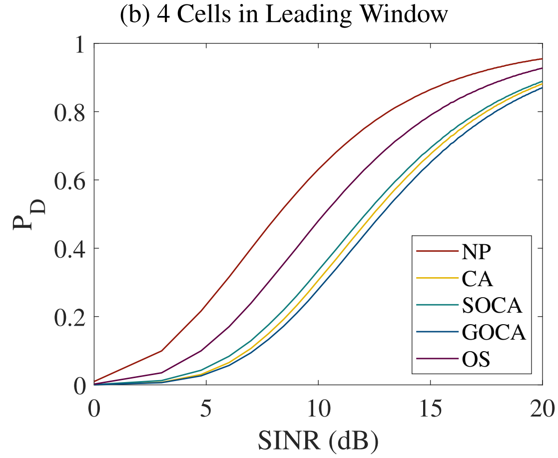

(d) 2 Cells in Leading and Lagging Windows

Figure 3.6: Clutter boundary scenarios, N_r = 12, N_g = 1

In Figure 3.6d, a clutter boundary was simulated in the leading and lagging windows. The SOCA detector produces a higher threshold due to the biased training cells in both windows, and performs similarly to the CA and GOCA detectors. The OS detector outperforms the CA, SOCA, and GOCA detectors because it omits clutter boundary cells regardless of their location in the CFAR window. The number of cells omitted by the OS detector strongly control its performance, as the OS detector would be expected to perform similarly to the other CFAR detectors as the number of clutter boundary cells were increased beyond 6.

It is important to note that the interference is assumed to have a mean value of 1 in the simulations shown in Figures 3.6a, 3.6b, 3.6c, and 3.6d to highlight the impact of clutter boundaries biasing the interference statistics estimate of each detector. The interference statistics are expected to increase as the clutter boundary dominates the CFAR window, but at different rates for each detector because the interference is nonhomogeneous in the leading and lagging windows. Remember that the threshold calculated by each CFAR detector is a product of their interference statistic estimate and their CFAR constant; a large interference statistic estimate will result in a large threshold, which decreases the P_D. The CA and GOCA detectors are expected to calculate a larger interference statistic estimate than the SOCA and OS detectors for the same set of test statistics in a CFAR window when a clutter boundary is present only in the leading window, which results in a lower P_D. The CA, SOCA, and GOCA detectors estimate a larger interference statistic estimate than the OS detector when a clutter boundary is present in the leading and lagging windows, resulting in the OS detector achieving the highest P_D.

Figure 3.7 shows the P_{FA} for each detector as a function of the clutter boundary cells in the leading window. The P_{FA} of the CA and GOCA detectors decrease rapidly as a result of their increased interference estimate, whereas the SOCA detector is only marginally affected by the clutter boundary. The OS detector decreases as the number of clutter boundary cells increases, but not as rapidly as the CA and GOCA detectors. The SOCA detector is likely to produce a low threshold when a clutter boundary is present in either the leading or lagging window, which results in a high P_D at the cost of an increased likelihood of false alarms from clutter boundaries. False alarms are extremely likely for the SOCA detector when the clutter boundary dominates the leading or lagging window and the CUT is the clutter boundary. The GOCA detector, however, was designed to choose the larger interference statistic estimate of the leading or lagging windows to combat false alarms at a clutter boundary, which degrades its detection performance overall. The OS detector can combat false alarms from clutter boundaries regardless of their position in the CFAR window and maintain a high P_D, making it the optimal detector of these clutter boundary scenarios.

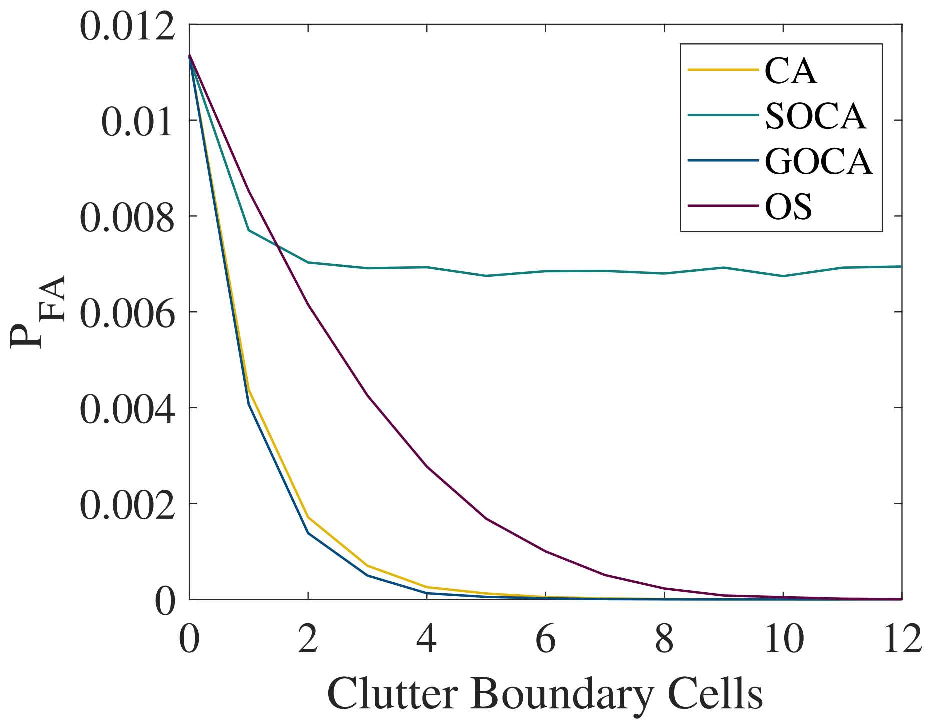

Figure 3.7: P_{FA} for each detector as the number of clutter boundary cells in the leading window is increased, N_r = 12, desired P_{FA} = 0.011

Figures 3.8a and 3.8b show P_D as a function of P_{FA} for each detector in two of the clutter boundary scenarios. In both clutter boundary scenarios, four of the 24 training cells have a mean value of 10. The results in Figure 3.8a are for each detector when all four clutter boundary cells are in the leading window, whereas in Figure 3.8b two cells are in the leading and lagging windows. The remainder of the CFAR window contained exponentially-distributed test statistics with a mean value of 1. Using (3.4), the P_D for each detector is calculated as

$$P_D = \exp\left(\frac{-T}{\hat{\sigma}_i^2 + \sigma_t^2}\right) \tag{3.23}$$

which resembles (3.5). The average threshold calculated by each detector was then substituted into (3.23) to relate P_D and P_{FA} for a target with a mean value 10 (i.e. $\sigma_t^2 = 10$). When the clutter boundary is limited to the leading window, the SOCA and OS detector outperform the CA and GOCA detectors. The GOCA detector likely produces the largest threshold of each detector, which degrades its detection when targets are near a clutter boundary. The performance of the SOCA detector is severely degraded when the clutter boundary is present in both windows, as seen in Figure 3.8b, but it performs marginally better than the GOCA detector because it chooses the smaller interference statistic estimate. The versatility of the OS detector is shown because it remains unaffected by the location of the clutter boundary in the training cells, and it achieves the highest P_D as a function of P_{FA} of each detector in these trials.

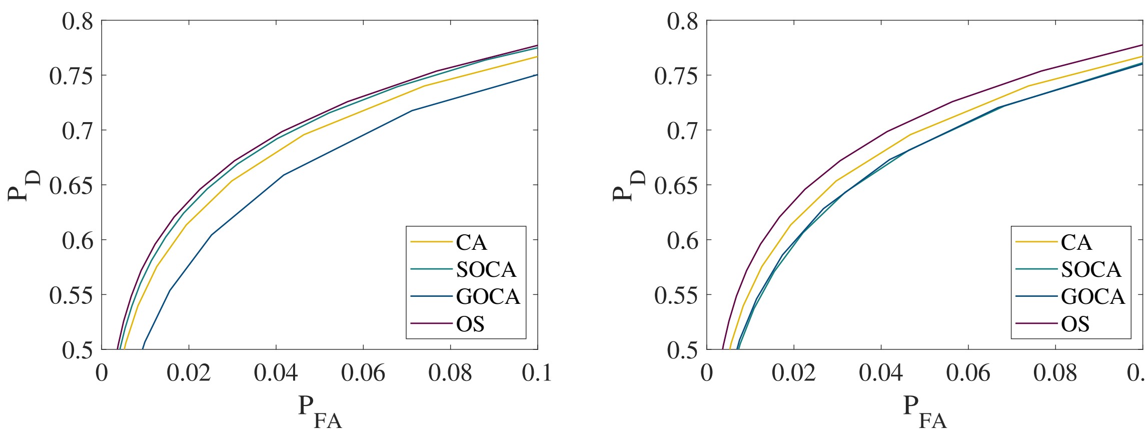

(a) 4 Cells in Leading Window

(b) 2 Cells in Leading and Lagging Windows

Figure 3.8: Clutter boundary in training window, N_r = 12

Another Monte Carlo simulation was conducted to investigate the performance of each detector in a target masking scenario. The interference in the CFAR window was simulated with a mean value of 1, and a target in the leading window was simulated with a mean value equal to the target in the CUT. The mean value of the targets were varied from 1 to 100, as shown in Figure 3.9. The OS and SOCA detectors perform best as they are designed to omit the target from the interference statistic estimate, and the CA and GOCA detectors are degraded as they do not omit the target from their interference statistics estimate. The impact of target masking is similar to a clutter boundary, except that the number of cells for target masking is generally less than the clutter boundaries and the clutter boundary's mean value is not varied. Additional analysis of target masking scenarios is omitted as it does not provide additional information about detector performance that has not been presented in the clutter boundary simulations.

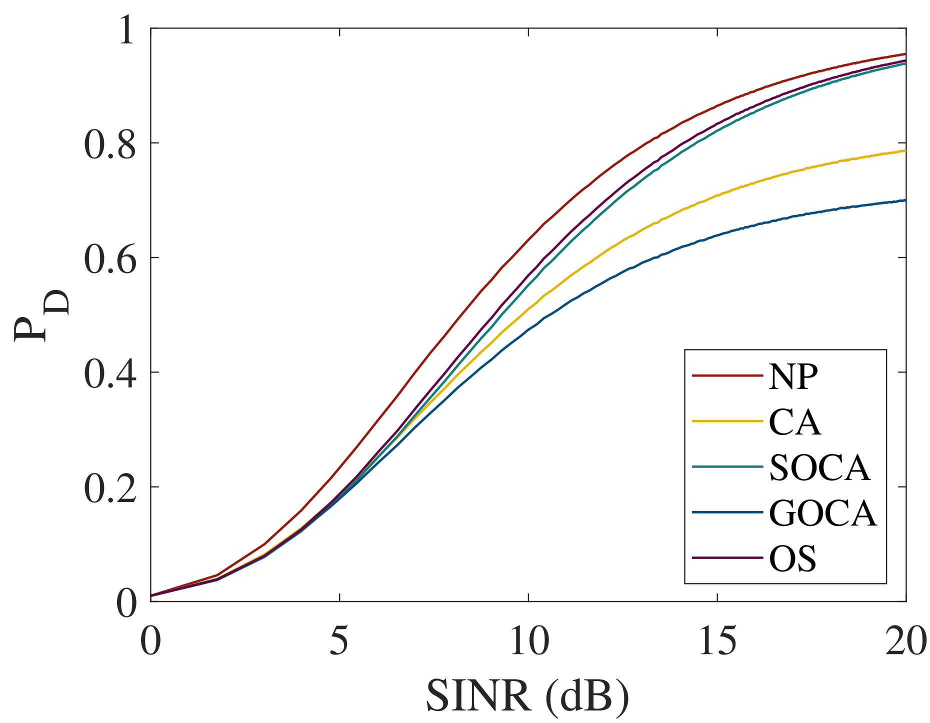

Figure 3.9: A target cell in the training cells with the same SINR as the target in the CUT, $N_r = 12$, $P_{FA} = 0.01$

The amplitude of clutter echoes from the Earth's surface near the surveillance radar can be much greater than the amplitude of the receiver's noise in radar measurements of the received signal, which can impact the distribution of the interference-only test statistics. As discussed in Section 2.3, the distribution of RCS values from rough clutter scatterers tends to follow a heavy-tailed distribution, such as the lognormal, K, or Weibull distributions. Interference cannot be modeled by a zero-mean complex Gaussian random process when non-Gaussian clutter echoes dominate the interference signal; instead, the PDF $p(y; \mathcal{H}_0)$ will resemble the clutter's RCS distribution and feature a heavy tail. The PDF of the lognormal distribution is written as [25]

$$p(x) = \frac{1}{x\sigma\sqrt{2\pi}} \exp\left[\frac{-1}{2}\left(\frac{\ln(x) - \mu}{\sigma}\right)^2\right] \tag{3.24}$$

where the expected value, or mean, is

$$E[x] = \exp\left[\mu + \frac{\sigma^2}{2}\right] \tag{3.25}$$

and its variance is

$$Var(x) = E[x^2] - E^2[x] = (\exp[\sigma^2] - 1)\exp\left[2\mu + \sigma^2\right]. \tag{3.26}$$

In Figure 3.10, a few variants of the lognormal distribution are plotted with the exponential distributions of the same mean, and the same distributions were plotted on a logarithmic scale in Figures 3.11a, 3.11b, and 3.11c. The likelihood of a lognormally distributed random variable taking on a large value is generally greater than that of an exponentially distributed random variable, which means that false alarms are expected to increase due to clutter echoes.

The functions relating a threshold, P_{FA}, and CFAR constant for the CA detector of Section 3.2 were derived assuming that the interference signal was exponentially distributed. The exponential distribution has only one statistical parameter: its mean value. As the PDF of the interference test statistics deviates from the exponential distribution, the accuracy of

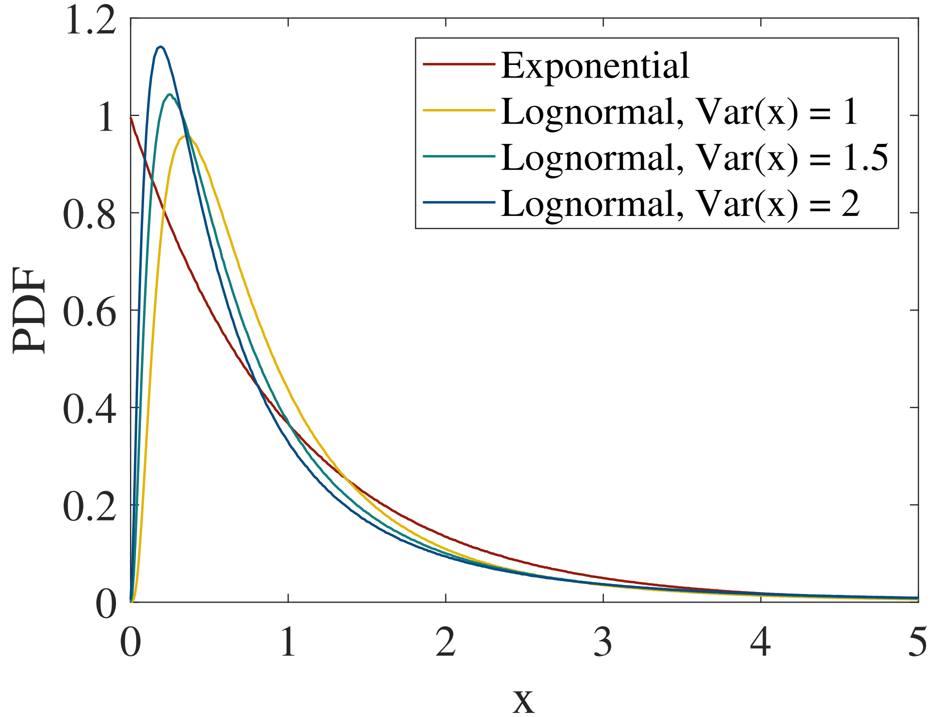

Figure 3.10: Histogram of exponential and lognormal RVs with the same mean value

the previous calculations is degraded. For example, the relationship between P_{FA} and a threshold for lognormally-distributed interference is provided as follows.

$$p(y;\mathcal{H}_0) = \frac{1}{y\sigma\sqrt{2\pi}} \exp\left[\frac{-1}{2}\left(\frac{\ln{(y)}-\mu}{\sigma}\right)^2\right] \tag{3.27}$$

Plugging $p(y;\mathcal{H}_0)$ from (3.27) into (3.2) and taking the complement of the lognormal distribution's cumulative distribution function as

$$P_{FA} = \frac{1}{2} - \frac{1}{2}\text{erf}\left(\frac{\ln{(T)}-\mu}{\sigma\sqrt{2}}\right) = -\frac{1}{2}\text{erfc}\left(\frac{\ln{(T)}-\mu}{\sigma\sqrt{2}}\right) \tag{3.28}$$

results in a P_{FA} and threshold relationship that depends on two parameters (μ and σ). Suppose that the CFAR window contains lognormal interference whose mean and variance are unknown. The CFAR detector can estimate the mean value of the interference in the

CFAR window to calculate a threshold, but the false alarm rate of the detector can increase if the variance parameter of the interference is large. The CFAR detectors in this work are designed to adjust the threshold as the mean value of the interference-only test statistics varies to stabilize the false alarm rate, but the detectors are not designed to estimate multiple unknown statistical parameters when calculating the threshold.

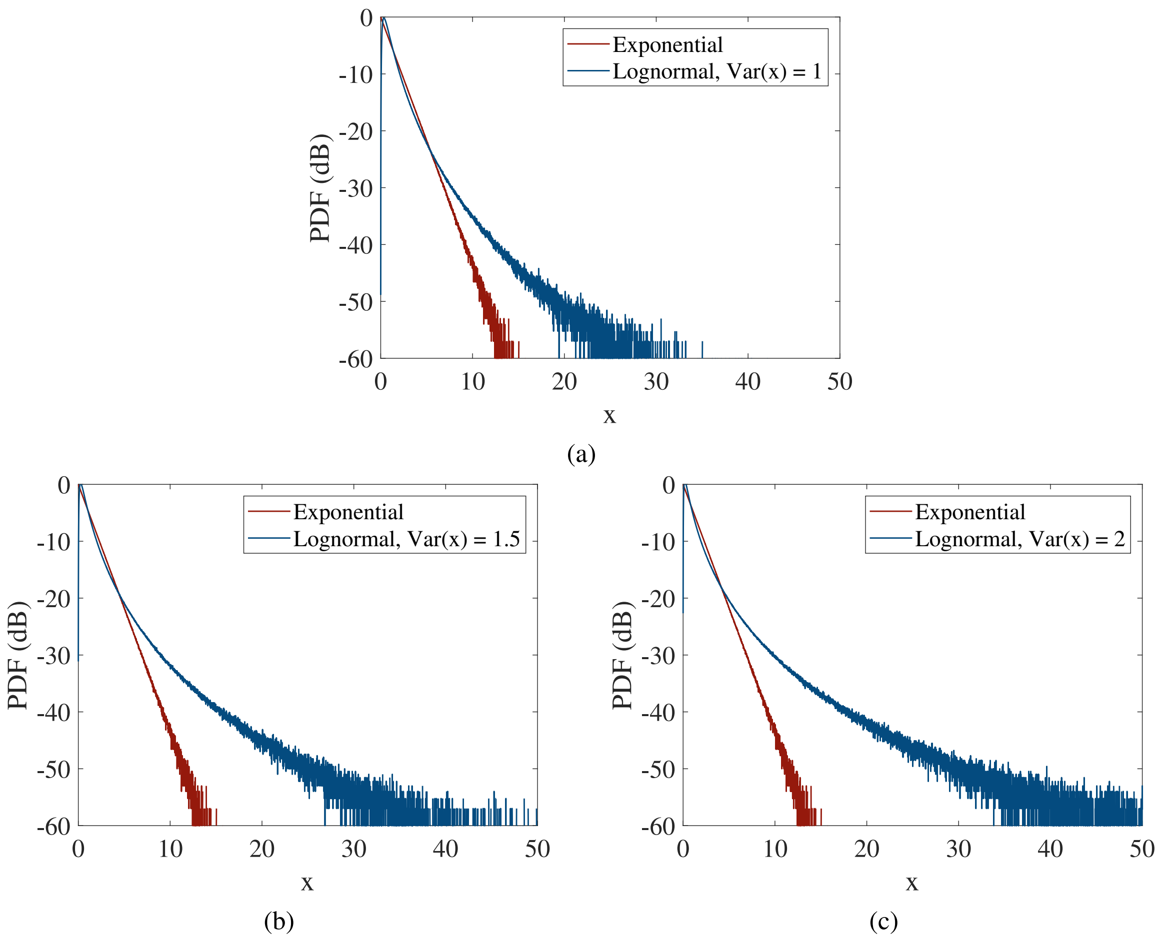

Figure 3.11: Logarithmic scale of exponential and lognormal distributions of the same mean value

A Monte Carlo simulation was conducted to compare the thresholds generated by the CA detector for exponentially and lognormally distributed interference with mean values of 1. The CFAR window was simulated to contain exponential interference for a million trials, and each calculated threshold was recorded. The distribution of thresholds produced by the CA detector is shown in Figure 3.12a, and it appears to follow a Gaussian distribution with a mean of 5. Additional simulations were conducted with lognormal interference in the CFAR window where the variance parameter was set to 1, 2, 5, and 10. When the variance parameter of the lognormal distribution is small, the distribution of thresholds produced by the detector appears similar to the distribution of thresholds produced when the detector processes exponential interference. As the variance parameter is increased, however, the threshold distribution deviates from the Gaussian distribution and the mean value of the thresholds increases as shown in Figures 3.12a, 3.12b, 3.12c, and 3.12d. The likelihood that a large realization from a lognormal random variable occurs increases as the variance parameter of the lognormal distribution increases. Therefore, lognormally distributed interference with a high variance parameter can increase the false alarm rate and decrease the probability of detection for a CFAR detector.

Additional Monte Carlo simulations were conducted to investigate how the variance parameter of the lognormal distribution impacts the threshold produced by each detector. When the variance parameter of the lognormal distribution is low, as it is in Figure 3.13a, the CA detector performs best. The likelihood of a lognormal random variable taking on a large value is low when its variance is low; for this reason, the CA detector produces the lowest average threshold when the variance parameter is less than 2. As the variance parameter of the lognormal distribution is increased (Figures 3.13a, 3.13b, 3.13c, and 3.13d), the likelihood of the interference taking on a large value also increases, and the CA detector's performance is degraded. A table of the average threshold produced by each detector in each variance trial is given in Table 3.1. The performance of the SOCA and GOCA detectors are also degraded as the variance parameter is increased because the lognormal interference impacts both the leading and lagging windows of the CFAR window. The OS detector is designed to remove large values from anywhere in the CFAR window when calculating the threshold, and thus it is able to produce the lowest average threshold as the

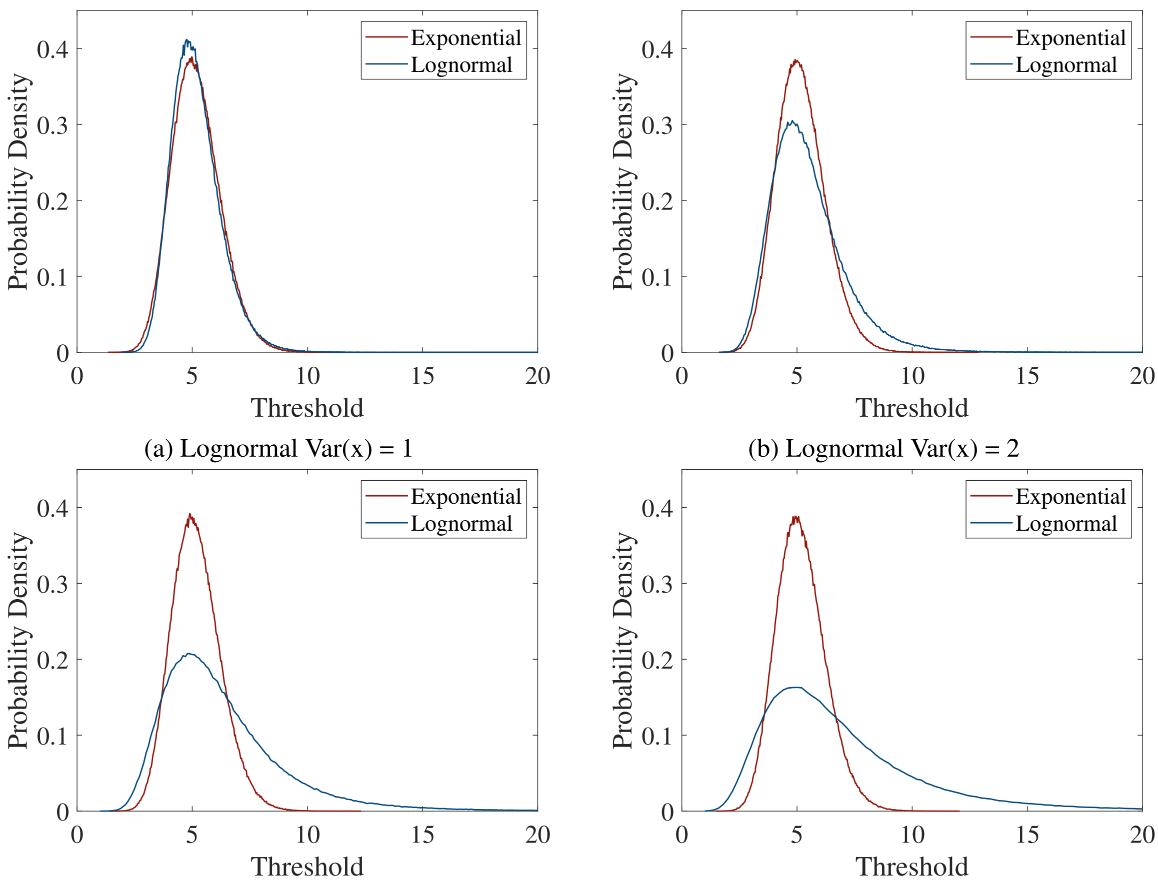

(a) Lognormal Var(x) = 1 (b) Lognormal Var(x) = 2

(c) Lognormal Var(x) = 5 (d) Lognormal Var(x) = 10

Figure 3.12: Histograms of CA detector thresholds for exponential and lognormal distributed interference, $N_r = 12$, $P_{FA} = 0.009$

variance of the interference is increased, resulting in the highest P_D of the simulated CFAR detectors.

	Var(x) = 1	Var(x) = 2	Var(x) = 5	Var(x) = 10
CA	4.91	5.47	6.35	7.26
SOCA	5.22	5.48	6.33	7.43
GOCA	5.28	5.83	6.91	8.39
OS	5.23	5.48	6.00	6.54

Table 3.1: Average threshold produced by each detector for different trials of lognormal interference

Additional Monte Carlo simulations were conducted to compare the performance of

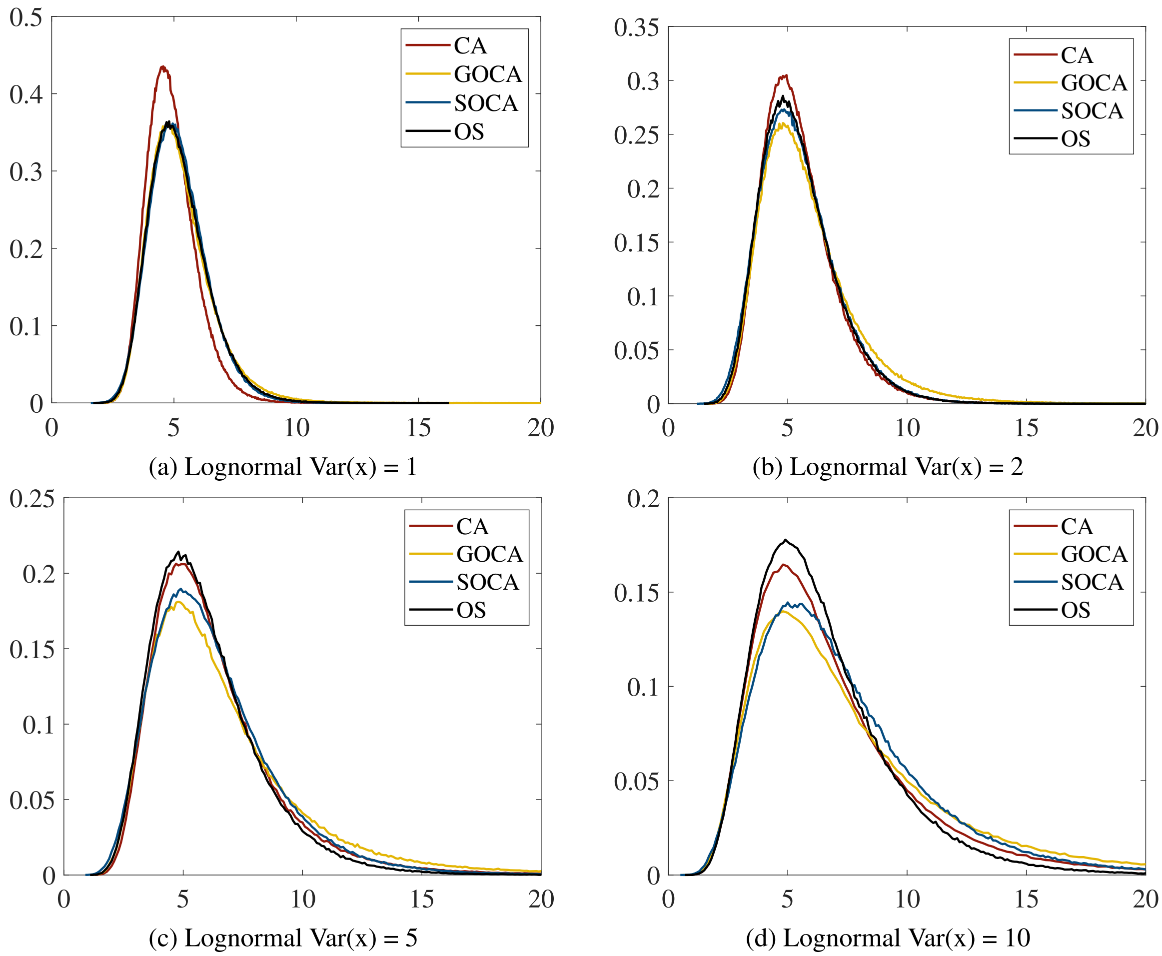

(a) Lognormal Var(x) = 1
(b) Lognormal Var(x) = 2
(c) Lognormal Var(x) = 5
(d) Lognormal Var(x) = 10

Figure 3.13: Histograms of CFAR detector thresholds for lognormal interference, $N_r = 12$, $P_{FA} = 0.01$

each detector on different variants of lognormal interference. In each trial, the CFAR window was simulated to contain lognormal interference with a mean value of 1 in the training cells and CUT. The P_{FA} was calculated for each trial, as the CUT was not simulated to contain a target. To determine P_D for each detector, the threshold generated by each interference statistic estimate was then plugged into

$$P_D = \exp\left(\frac{-T}{\sigma_t^2}\right) \tag{3.29}$$

which is the P_D for an exponentially distributed target, but excludes the σ_i^2 term from

(3.23) because the interference is lognormal. The target model was simplified because the distribution for an exponentially distributed target in lognormally distributed interference does not have a closed-form solution. The value of σ_t^2 was set to 10 for these trials. The CA detector performs best when the variance of the lognormal interference is low, but the OS detector becomes the optimal detector for lognormal interference as the variance increases. The OS detector performs best of all detectors in this simulation because it omits large spikes produced by the lognormal random variable that degrade the detection performance of the CA, SOCA, and GOCA detectors regardless of their position in the CFAR window.

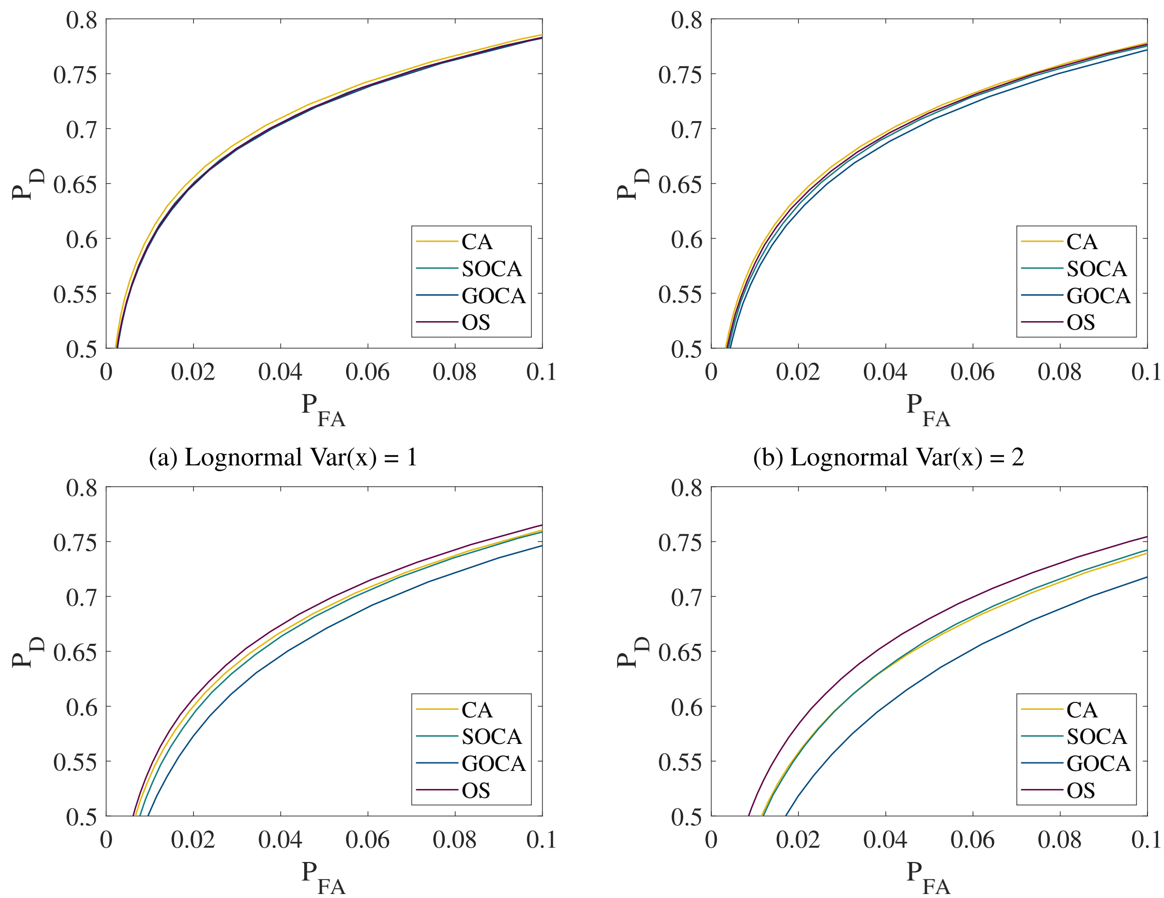

(a) Lognormal Var(x) = 1

(b) Lognormal Var(x) = 2

(c) Lognormal Var(x) = 5

(d) Lognormal Var(x) = 10

Figure 3.14: CFAR detector performance on lognormal interference of different variance values, $N_r = 12$

Chapter 4

Simulation & Results

The simulated data presented in this work are intended to be representative of the data produced by a ground-based, mechanically steered surveillance radar. Radars receive a signal that contains interference, namely thermal noise, electromagnetic interference, and clutter echoes, and may contain target echoes. Electromagnetic interference is acknowledged as a source of interference in the received signal, as it degrades the detection performance of surveillance radar systems, but its modeling and simulation fall outside the scope of this work. The simulation of the received signal is therefore limited to producing thermal noise, clutter echo, and target echo signals. A processing chain is implemented in the simulation to maintain the energy of target echo signals and reduce the energy of interference signals, thereby increasing the SINR of the received signal and probability of target detection. The processing chain converts the simulated received signal into test statistics, which are compared to a threshold to determine whether the received signal contained interference alone or interference and a target echo. Various CFAR detectors were implemented in the simulation to process the test statistics, and which allows for an analysis of CFAR detector performance when the received signal contains nonhomogeneous interference.

4.1 Ground-Based Surveillance Radar Data Simulation

The boresight of the simulated radar's antenna was set at a constant elevation angle below the horizontal plane and rotated about the vertical axis at a rate of ω revolutions-per-minute to illuminate targets and surface clutter surrounding the radar. Pulse transmissions were staggered to reduce the impact of blind speeds in the processed radar measurements, which is common for surveillance radars, and the antenna radiation pattern illuminating the scene of interest was calculated pulse-by-pulse. Although additional antenna beams can be modeled to simulate a radar scanning for targets above the horizontal plane, the simulation is limited to where the interference signal is expected to contain surface clutter echoes. Not only does the omission of additional antenna beams focus the study to nonhomogeneous sources of interference, but it also keeps the simulation computationally manageable.

The Price NLFM waveform discussed in Section 2.1 was chosen to represent the radar signal because it features low ACF sidelobes and maintains a high Doppler tolerance, which are desirable qualities for a radar signal used in detection applications. A radar signal's echo can be simulated by time-delaying, amplitude-scaling, and Doppler-shifting a copy of the transmitted radar signal. The time delay, amplitude scale, and Doppler shift of the radar signal's echo correspond to the radial range between the scatterer and the radar, physical characteristics of the scatterer, and relative motion between the scatterer and the radar, respectively. Target echo signals are simulated as reflections from point targets, or scatterers whose physical size is much smaller than the range and angular resolutions ($\Delta R, \theta_3$, and ϕ_3) of the radar system. The target echo signal, $s(t;\theta_p)$, as a function of time and antenna angle, is given by (2.52) and rewritten here as

$$s(t;\theta_p) = \alpha_t(\tau,\theta,\phi;\theta_p)\,\tilde{x}(t-\tau)\,\exp\left(j2\pi f_D t\right). \tag{4.1}$$

The physical size of surface clutter extends beyond the range and angular resolutions of the radar system, and thus the clutter echo signal is the sum of the reflections from each differential scatterer (with area dA) on the clutter surface as (2.54), which is rewritten below

$$w_c(t;\theta_p) = \int \int_{\Delta A} \alpha(\tau, \theta, \phi; \theta_p)\, \tilde{x}(t-\tau) \exp\left(j2\pi f_D t\right) dA d\tau. \tag{4.2}$$

A flat, continuous clutter surface was modeled in the simulation by dividing the surface into surface patches, as depicted in Figure 4.1. The area of a patch in Figure 4.1 is of the form $A = R\Delta\theta\Delta R$, where R is the range to the patch, ΔR is the width of the patch in range, and $R\Delta\theta$ is the length of the arc. To accurately model the echoes from continuous surface with clutter patches, the surface area of each clutter patch must be smaller than the range and angular resolutions of the radar (ΔR and θ_3). Therefore, the width of each clutter patch was chosen to be four times smaller than the range and angular resolutions of the radar model, which corresponds to 16 clutter patches per resolution cell. The surface area of each clutter patch (A) in the model was calculated by

$$A = \frac{R\theta_3\Delta R}{16 \cos \delta}, \tag{4.3}$$

which resembles (2.48) because the radar simulation was resolution limited. The cos δ term accounts for the grazing angle of the scatterer because the radar is positioned at some height above the surface. The natural terrain of the Earth's surface is generally rough, and the RCS of rough clutter surfaces tend to follow heavy-tailed distributions, such as the lognormal, K, or Weibull distributions. Using (2.43), the RCS of each clutter patch (σ) was found by multiplying its surface area (A) by its scattering coefficient (σ^0). To model the stationary surface clutter signal, the integral definition of (2.57) is approximated as

$$w_c(t, \theta_p) \approx \sum \sum \alpha(\tau_l, \theta_m, \phi_n; \theta_p)\tilde{x}(t-\tau_l)\Delta\theta\Delta\tau \tag{4.4}$$

where $\Delta\tau$ and $\Delta\theta$ are based on the size of the clutter patches in range (using (2.26))) and azimuth ($\theta_3/4$).

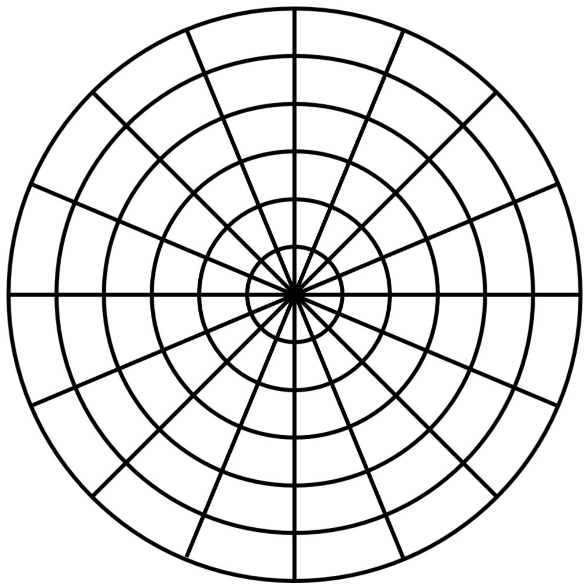

Figure 4.1: Top-down view of a surface divided into patches

The radar system was simulated to rotate at a low rate of revolution, and, in some simulation trials, the system did not even complete a full revolution. In the interest of maintaining a computationally efficient simulation, the reflections modeled were limited to targets and clutter patches within $\pm 90°$ of the antenna's boresight (in azimuth and elevation) from the first and final pulse transmission. In other words, only the mainlobe and sidelobes of the antenna were modeled while the backlobes were excluded. In Figure 4.2a, the RCS values of each simulated clutter patch is shown for a trial that only scanned $\approx 20°$ across azimuth. In Figure 4.2b, the antenna radiation pattern for the first pulse is shown over the grid of clutter patches, which is used to calculate the amplitude of the pulse echoes from targets and surface clutter patches (along with their RCS and range using (2.38)).

The received signal is the superposition of the time-delayed, amplitude-scaled, and Doppler-shifted wave echoes from targets and surface clutter along with additive thermal noise from the radar's receiver. The random thermal motion of the electrons in the radar's

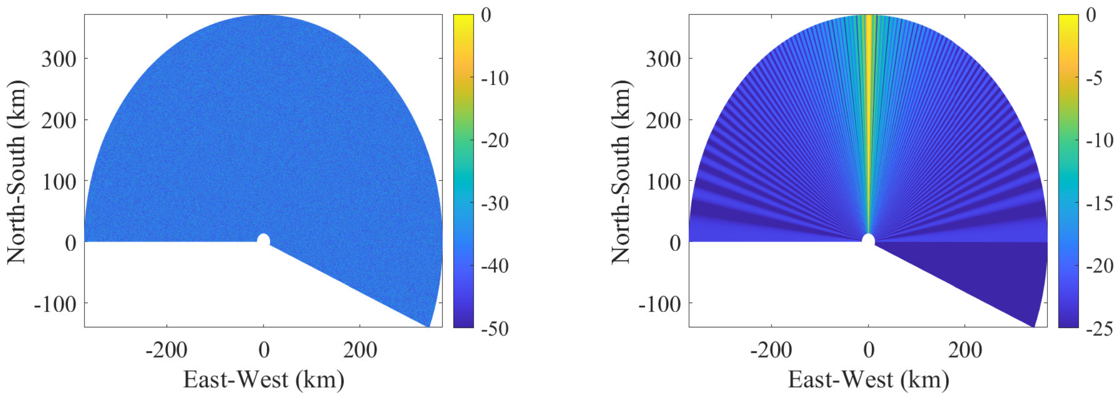

(a) RCS of Surface Clutter Patches

(b) Antenna Radiation Pattern

Figure 4.2: A scene of clutter patches with lognormally distributed RCSs and the antenna radiation pattern illuminating the scene

receiver was modeled as a zero-mean, complex Gaussian additive random process with a noise power of P_n. The received signal was sampled by the radar's receiver into radar measurements and then matched filtered to increase the SNR of target echoes. An example range profile of radar measurements taken from a single pulse are shown in Figures 4.3a and 4.3b, where both figures show the magnitude of the received signal as a function of range. The radar range equation features an R^4 term in the denominator due to the two-way propagation of the radio wave, which strongly impacts the amplitude of a scatterer's echo signal received by the radar as its range increases. Only thermal noise and clutter echoes were simulated in this trial, and for this example, clutter echoes dominate the received signal up to ≈ 50 km. Thermal noise, however, does not have a range dependence and affects all radar measurements and dominates the received signal for ranges greater than ≈ 50 km.

After a set of radar measurements has been collected from a series of pulse transmissions and then matched filtered, the processing chain begins filtering the clutter echoes from the radar measurements. The FFT cannot be used to pulse-Doppler process the radar measurements into a range-Doppler map due to the staggered pulse transmissions. An

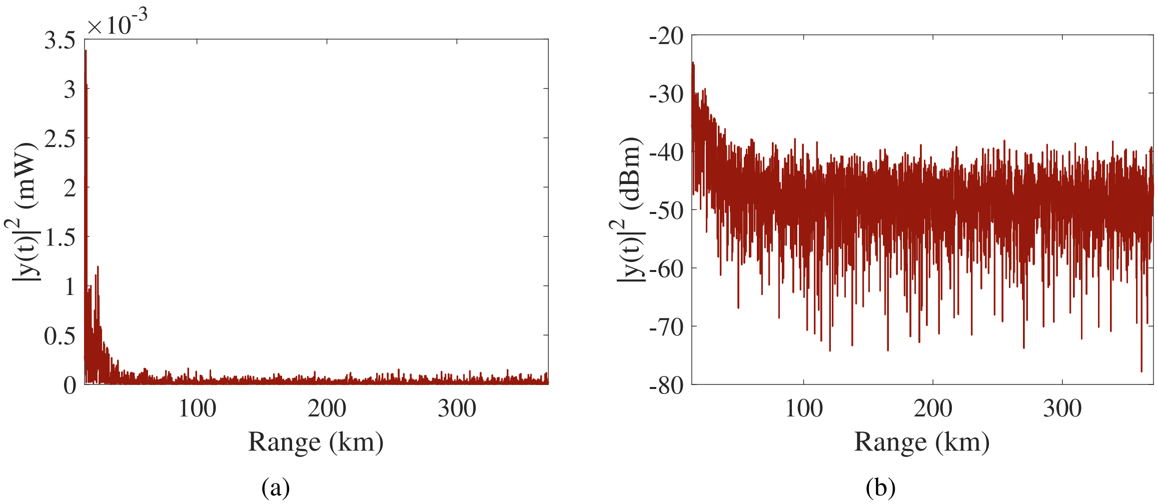

Figure 4.3: Example range profiles for radar measurements taken after a single pulse was transmitted. Shown in mW (a) and dBm (b).

algorithm may be designed using a modified DFT to account for the non-uniform pulse intervals, but it is not feasible for implementation on computationally-limited systems, such as legacy radar systems. Instead, an N-pulse canceller performs well as a clutter filter at a much lower computational cost than pulse-Doppler processing. An 8-pulse canceller was modeled in the system, and the squared magnitude of its average frequency response is shown in Figure 4.4. The clutter filtering performance of the 8-pulse canceller is shown on a range profile of radar measurements in Figures 4.5a and 4.5b. In this trial, a target 40 km from the radar was simulated and the target becomes more distinguishable from clutter echoes at the output of the clutter filter.

The next stage of the processing chain involves compressing the dynamic range of the input radar measurements. The radar measurements at the output of the clutter filter are the input values for a simulated logarithmic amplifier. The output (y) of the simulated logarithmic amplifier is characterized by the following

$$y = \sqrt{\log_2(|\text{real}(x)| + 1)^2 + \log_2(|\text{imag}(x)| + 1)^2} \tag{4.5}$$

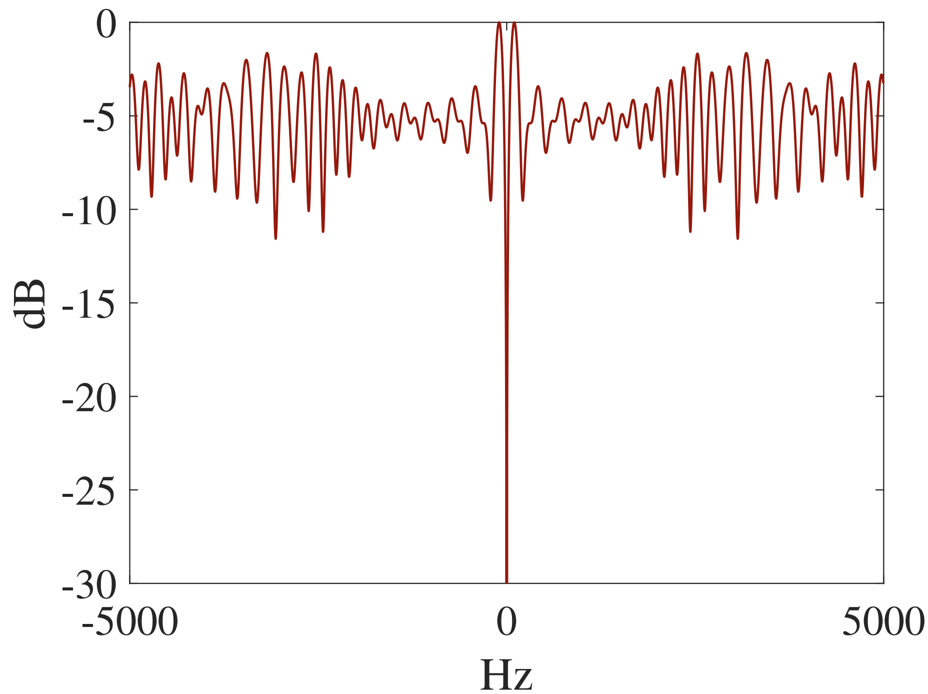

Figure 4.4: The squared magnitude of the average frequency response from an 8-pulse canceller with a staggered PRF input

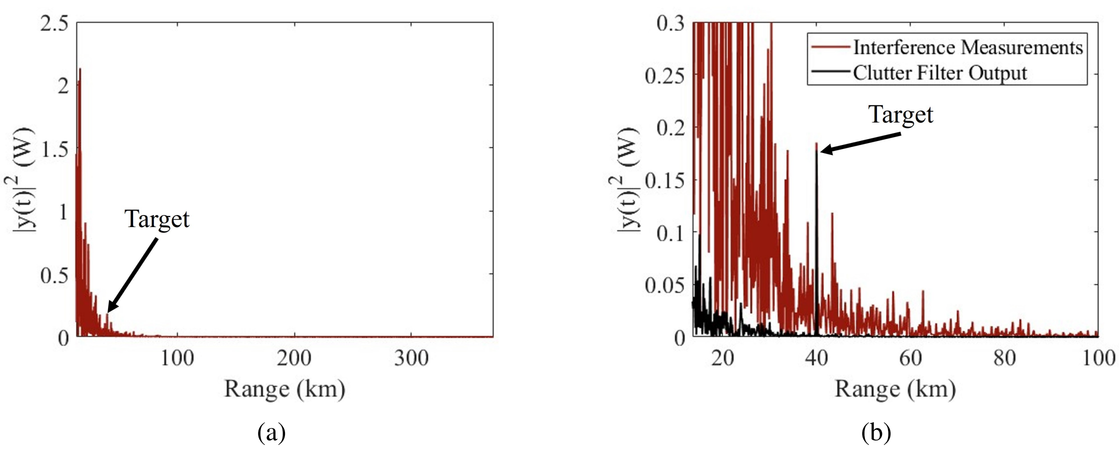

Figure 4.5: Range profile before and after the clutter filter is applied in (a) and enhanced in (b)

where x is the input to the amplifier. The "$+ 1$" terms are intentionally included in (4.5) to prevent the simulated amplifier from erroneously amplifying input values close to 0 to large values and to avoid $\log_2(0)$ from occurring. The input/output relationship of the simulated amplifier is shown in Figure 4.6, where it is plotted alongside simulated linear ($y = x$) and squared magnitude ($y = |x|^2$) amplifiers. Note that the output data from logarithmic amplifier implemented in this simulation is different than the log-magnitude data produced by the logarithmic amplifier described by (2.69) which converts an amplitude to a decibel value. The output of the dynamic range compression stage of the processing chain is shown in Figure 4.7.

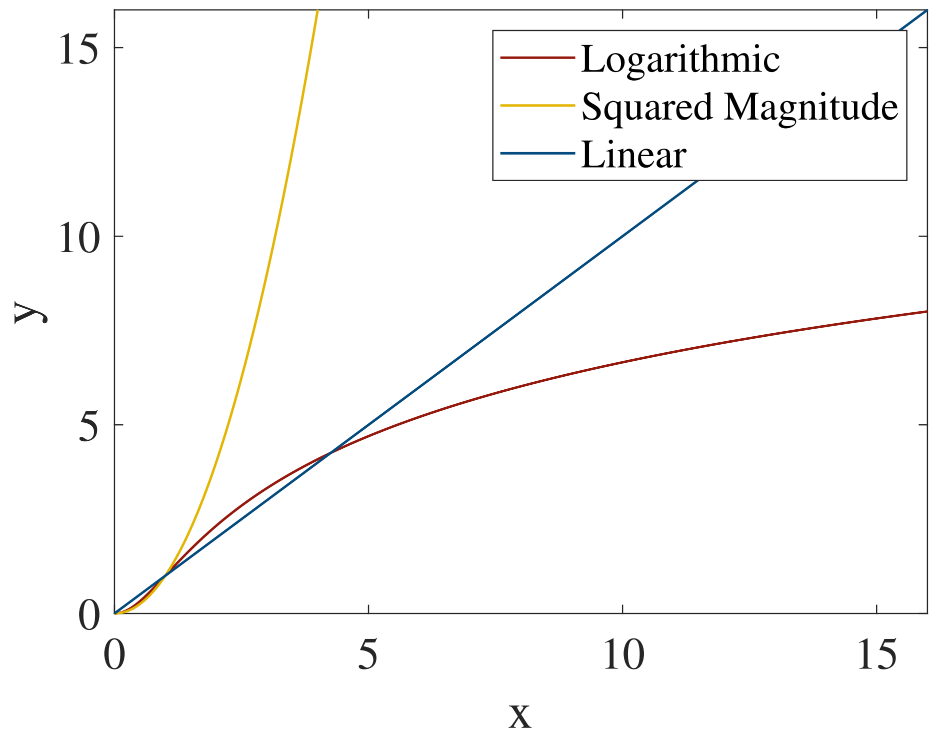

Figure 4.6: Input and output relationships of example linear, squared magnitude, and logarithmic amplifiers

The final stage of the processing chain involves the noncoherent integration of radar measurements across the slow-time dimension. The noncoherent integrator is implemented to sum the radar measurements at the output of the logarithmic amplifier to achieve an integration gain for target echo signals, and therefore increase their SNR and detectability. The integrator was designed to sum eight contiguous slow-time radar measurements for each range bin, and its output is shown in Figure 4.8. The SNR of a target is defined as the

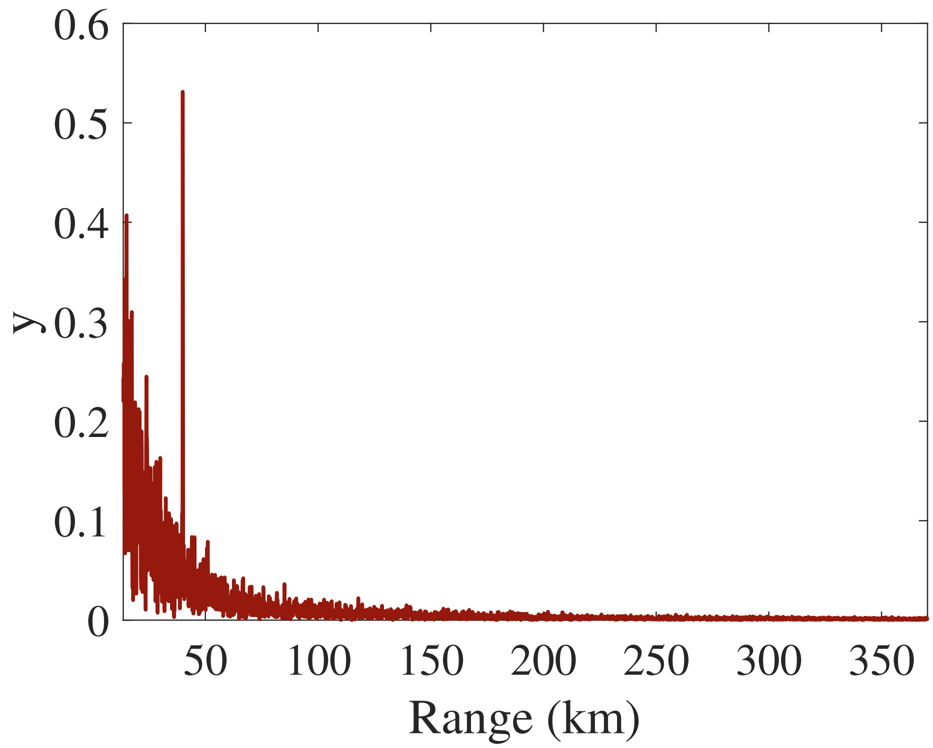

Figure 4.7: Output of the dynamic range compressor

ratio of the expected power reflected by a target to the receiver's thermal noise power, or

$$\text{SNR} = \frac{P_t G^2 \lambda^2 \sigma}{(4\pi)^3 R^4 k T_0 B F}. \tag{4.6}$$

As discussed in Section 2.5, a coherent radar system that implements a slow-time pulse integrator in its processing chain should expect a SNR integration gain of M, while a noncoherent system should expect a SNR integration gain of $\approx \sqrt{M}$, where M corresponds to the number of measurements summed (M = 8 for this example). The simulated received signal contains clutter echo signals, so the more important metric to determine a target's detectability is the SINR. The SINR of a target is defined similarly to SNR, but it includes the total interference power in the received signal as

$$\text{SINR} = \frac{\frac{P_t G^2 \lambda^2 \sigma}{(4\pi)^3 R^4}}{kT_0BF + P_c} \tag{4.7}$$

where P_c is the clutter echo power defined by the squared magnitude of (2.54).

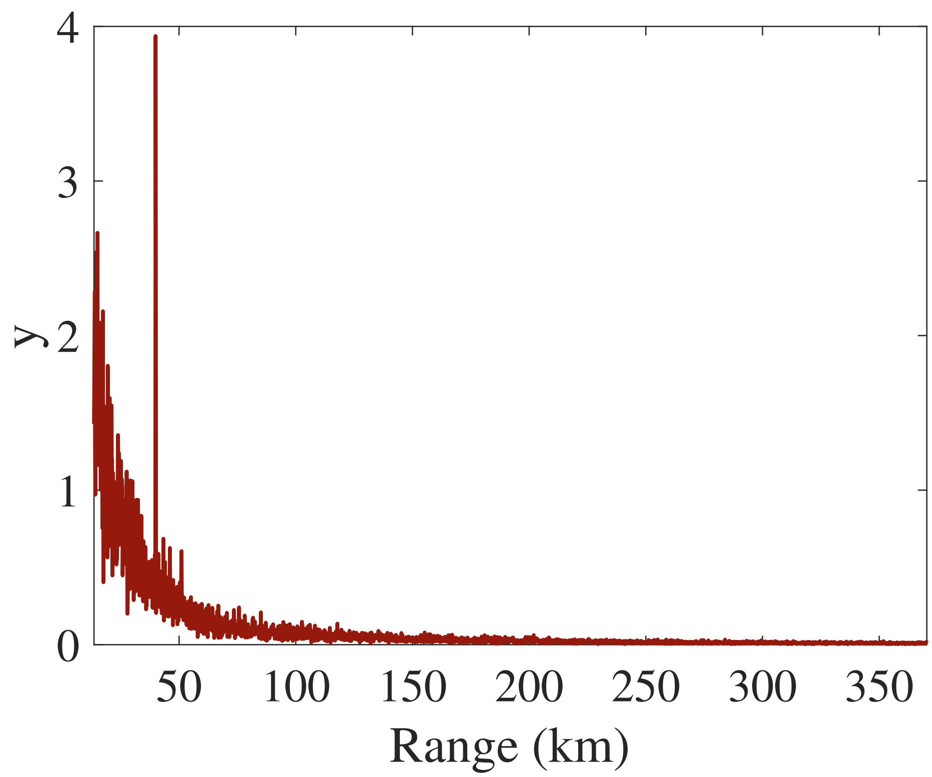

Figure 4.8: Output of the noncoherent integrator

The SINR and noncoherent integration gains are not easily quantifiable in this simulation due to the complex nature of the logarithmic amplifier and clutter filter stages from the processing chain. To begin estimating the SINR and noncoherent integration gains, the peak value of the target echo (S) and the peak value from a clutter echo (P_c) near the target were recorded along with the average interference signal (N) from ranges greater than 200 km. These values were measured before and after noncoherent integration, and then psuedo-SNR and psuedo-CNR (clutter-to-noise ratio) quantities were calculated. The expression for SNR can be written as S/N, the CNR as P_c/N, and SINR can be written as S/(N+P_c). Before noncoherent integration, SNR = 366.67, CNR = 193.32, and SINR = 1.89, and after noncoherent integration, SNR = 314.29, CNR = 133.34, and SINR = 2.34. Although the SNR did not increase in this example, the target's SINR increased by 23.8% because the SNR decreased less than the CNR after noncoherent integration. It is important to note that the previous calculations were performed on only the noncoherent integrator stage, and the SINR of the target increased by a much larger percentage than 23.8% overall due to the entire processing chain.

The target's SNR likely did not increase at the output of the noncoherent integrator due to the logarithmic amplifier stage before the noncoherent integrator. Richards indicated in [2] that the integration gain is much more complex to calculate due to cross terms between interference and target echo signals (as discussed in Section 2.5), but it is also noted that the "$+\ 1$" terms added to prevent log(0) from occurring in the simulation likely induces an offset to the data in the processing chain. As a result, the S, P_c, and N terms increase almost equally in the noncoherent integrator stage, which inhibits the SNR of the target from increasing. Although it did not improve the SNR of the target in this example, the noncoherent integrator was not removed from the simulated processing chain in order for the processing chain to be consistent with that of a typical surveillance radar system.

4.2 Simulated Data Analysis

Additional range profiles were simulated featuring no targets to investigate the statistical behavior of the surface clutter model. The exclusion of targets from these trials ensures that the radar measurements (and test statistics) contained interference-only. In the first trial, the scattering coefficient (σ^0) of the simulated clutter patches were assigned a value from an exponential random variable with a mean of 1. The second, third, and fourth trials were conducted where the scattering coefficients of the clutter patches were lognormally distributed with a mean value of 1 and a variance of 5, a mean value of 1 and a variance of 50, and a mean value of 1 and a variance of 100. In order for the clutter echo signal to retain lognormal statistics (i.e. feature a heavy tail) after the processing chain, the variance of the lognormal random variable assigned to the scattering coefficient of each clutter patch must be large valued. If the variance was chosen to be too small, very few clutter patches with large RCS values would be generated in the simulation. Due to the random sum of clutter patch echo signals with similar RCS values, the received signal would tend to a complex Gaussian distribution (due to the central limit theorem [3]), and the squared magnitude of radar measurements would be exponentially distributed.

For each of the four trials examined, clutter echoes strongly impact the interference statistics of the radar measurements and test statistics in the region from R_{min} to 50 km. The distribution of radar measurements (squared magnitude) from R_{min} to 50 km are shown in Figures 4.9a and 4.9c, and the distribution of test statistics (after processing chain) from R_{min} to 50 km are shown in Figures 4.9b and 4.9d. In Figures 4.9a and 4.9c, it can be seen that the radar measurements from clutter patches whose scattering coefficients are lognormally distributed produce a heavier-tailed distribution than those from clutter patches whose scattering coefficient is exponentially distributed. In Figure 4.10, the distributions of the radar measurements from exponential clutter and a couple of the lognormal variants are plotted on a logarithmic scale.

The range profiles for each of the previous four trials are shown in Figure 4.11 and Figures 4.12a-4.12d, where an additional variant of the lognormally distributed scattering coefficients is shown (its mean is 1 and variance is 10). The range profiles with the fewest outliers are generated by the trial with clutter patches whose scattering coefficient is exponentially distributed (Figure 4.11). The range profile with the next fewest outliers is from the trial where the scattering coefficients are lognormally distributed with a variance

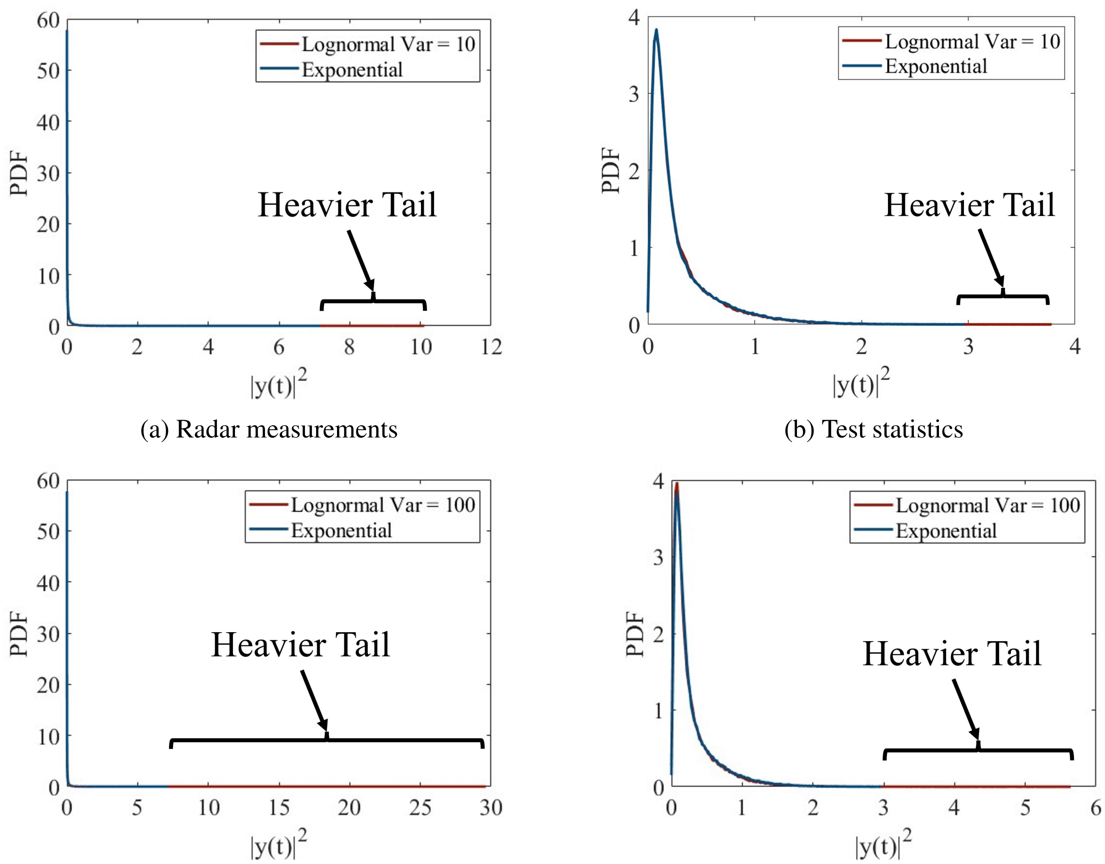

(a) Radar measurements

(b) Test statistics

(c) Radar measurements

(d) Test statistics

Figure 4.9: Distribution of radar measurements (a) and test statistics (b) from the clutter dominant region of the range profile (R_{min} to 50 km)

of 5 (Figure 4.12a), and it is noted that the range profiles closely resembled the exponential case. As the variance of the lognormal random variable is increased, the likelihood of a clutter patch taking on a large RCS value is increased, which explains the trend of increased outliers in Figures 4.12b, 4.12c, and 4.12d.

4.3 CFAR Detector Comparison

A few metrics were recorded to evaluate the performance of each detector on the simulated surveillance radar data. The first metric is the average threshold produced by each

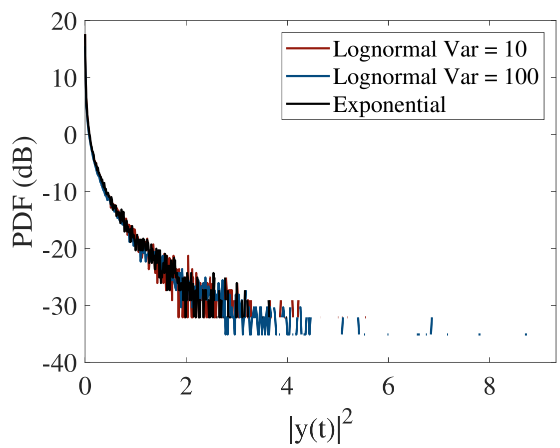

Figure 4.10: Distribution of radar measurements from the clutter dominant region of the range profile (R_{min} to 50 km) on a logarithmic scale

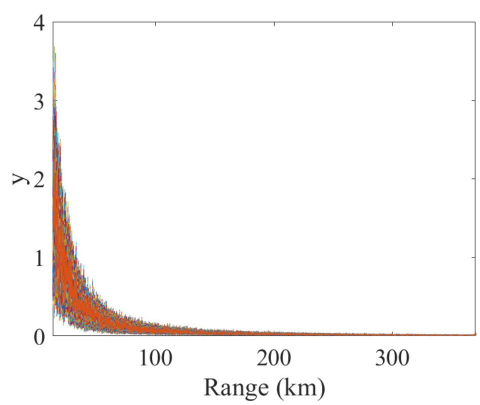

Figure 4.11: Range profile, exponentially distributed scattering coefficients

detector on the simulated data. The CFAR detector able to produce the lowest average threshold for a given P_{FA} is the optimal detector for that P_{FA}, as low thresholds are correlated to high P_D. The next metric relates the P_D to P_{FA} for each CFAR detector, also referred to as receiver operating characteristic curves [2]. No targets were simulated in these trials (in order to retain the lognormal or exponential statistics), and thus any detections are false alarms and P_{FA} is easily measured. The P_D for each detector was calculated by plugging the threshold generated in each simulation into (3.29), where $\sigma_t^2 = 3$. The simulated test statistics produced from the range profiles in Section 4.2 were processed by

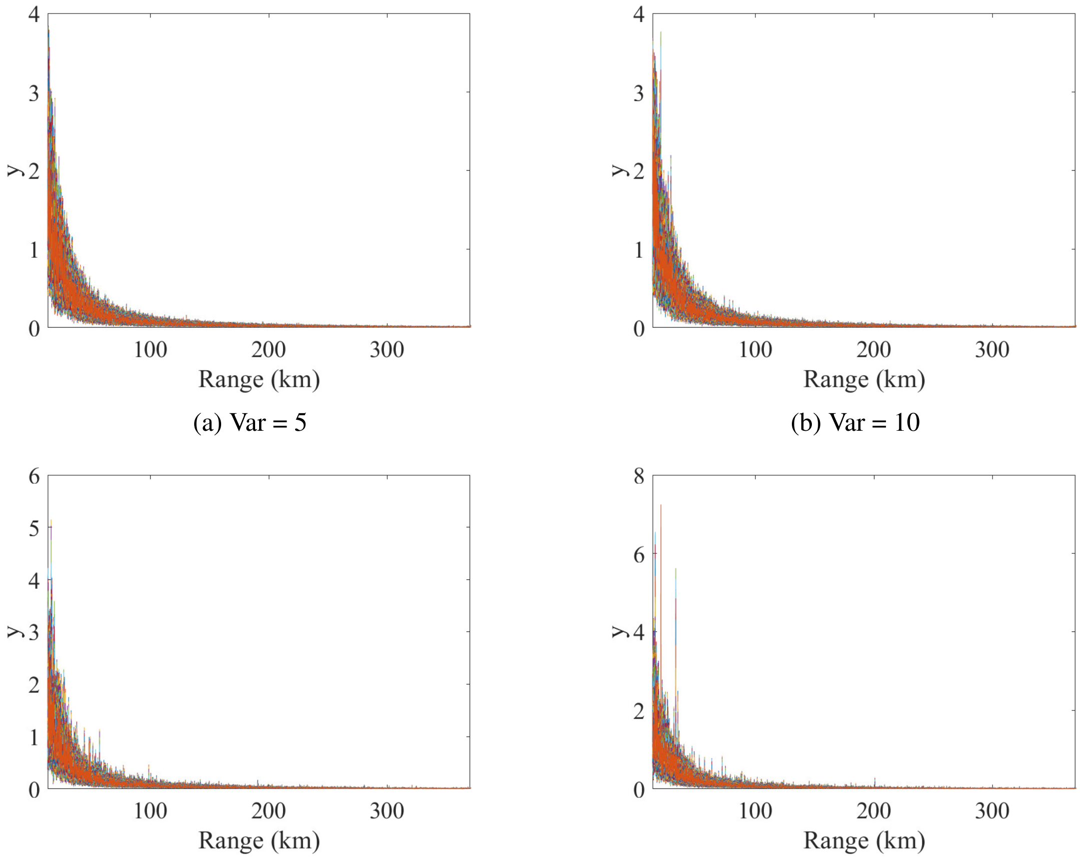

(a) Var = 5

(b) Var = 10

(c) Var = 50

(d) Var = 100

Figure 4.12: Range profiles for variants of lognormally distributed scattering coefficients

the CA, SOCA, GOCA, and OS detectors. The CFAR constants for each detector were designed to achieve a P_{FA} of 0.1, and the number of training cells in the CFAR windows was $N = 2N_r = 12$.

The thresholds calculated by each detector were recorded for the trial where clutter patches were modeled with an exponentially distributed scattering coefficients. The distribution of thresholds calculated by each detection is shown in Figure 4.13, and the mean value of the thresholds calculated are recorded in Table 4.1. The mean value of the thresholds calculated for test statistics from R_{min} to 50 km were recorded in Table 4.2 as an additional metric, because this region is where clutter echoes are expected to dominate the received signal. The CA detector performs best when the test statistics in the CFAR window are homogeneous and exponentially distributed. The test statistics are not exponentially distributed at the output of the processing chain, but the distribution of the test statistics closely resembles the exponential distribution. Additionally, the value of N was set to a low value such that the test statistics in the CFAR window could be locally homogeneous. The CA detector thus performs the best of the CFAR detectors in this trial, as it achieved the lowest average threshold.

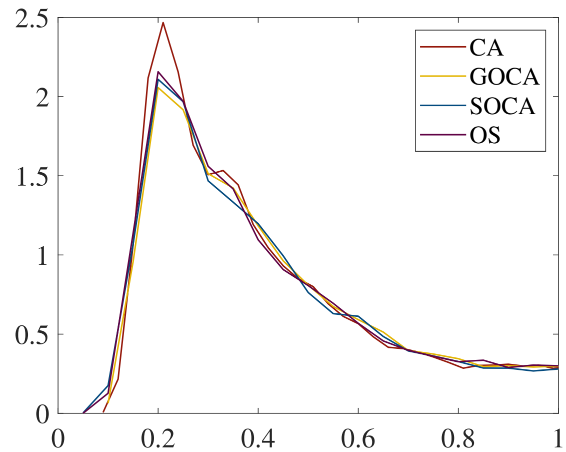

Figure 4.13: Distribution of thresholds calculated by each CFAR detector on simulated range profiles containing exponential interference

CA	SOCA	GOCA	OS
0.1537	0.1637	0.1671	0.1608

Table 4.1: Average threshold produced by each detector for different trials of exponential interference, whole range profile

CA	SOCA	GOCA	OS
0.7074	0.7540	0.7681	0.7387

Table 4.2: Average threshold produced by each detector for different trials of exponential interference, R_{min} to 50 km

Next, the thresholds calculated by each detector were recorded for the trials where the clutter patches were modeled with variants of the lognormal distribution. The distribution of thresholds calculated by each detector are shown in Figures 4.14a, 4.14b, 4.14c, and 4.14d. The mean value of the thresholds calculated from the test statistics throughout the whole range profile are recorded in Table 4.3, and the mean value of the thresholds calculated for test statistics from R_{min} to 50 km were recorded in Table 4.4. The range profile in the first lognormal trial, where the variance is 5, resembles the range profile from the previous trial where the scattering coefficients of the clutter patches was an exponential random variable. The range profile features marginally more statistical outliers, which explains why the CA detector does not perform as well as it had in the previous trial, but the CA detector was determined to be the best detector for the first lognormal trial. In the subsequent lognormal scattering coefficient trials, the CA detectors performance is degraded; as the variance of the lognormal random variable increases, the tail of the distribution becomes heavier. The OS detector was the optimal detector for the remaining lognormal trials, as it produced the lowest average threshold for variances of 10, 50, and 100. The SOCA detector performs nearly as well in the variance = 10 trial, but its average threshold was marginally larger. The design of the OS detector allows for statistical outliers, such as large returns from clutter echoes, to be omitted from anywhere in the CFAR window. The SOCA detector is limited to omitting a leading or lagging window, which can degrade its detection performance if statistical outliers are present in the leading and lagging windows. Thus, the OS detector performs best overall when compared to the CFAR detectors from these lognormal clutter trials.

	Var(x) = 5	Var(x) = 10	Var(x) = 50	Var(x) = 100
CA	0.1606	0.1693	0.1721	0.1785
SOCA	0.1620	0.1625	0.1646	0.1703
GOCA	0.1672	0.1766	0.1813	0.1892
OS	0.1608	0.1619	0.1624	0.1635

Table 4.3: Average threshold produced by each detector for different trials of lognormal interference, whole range profile

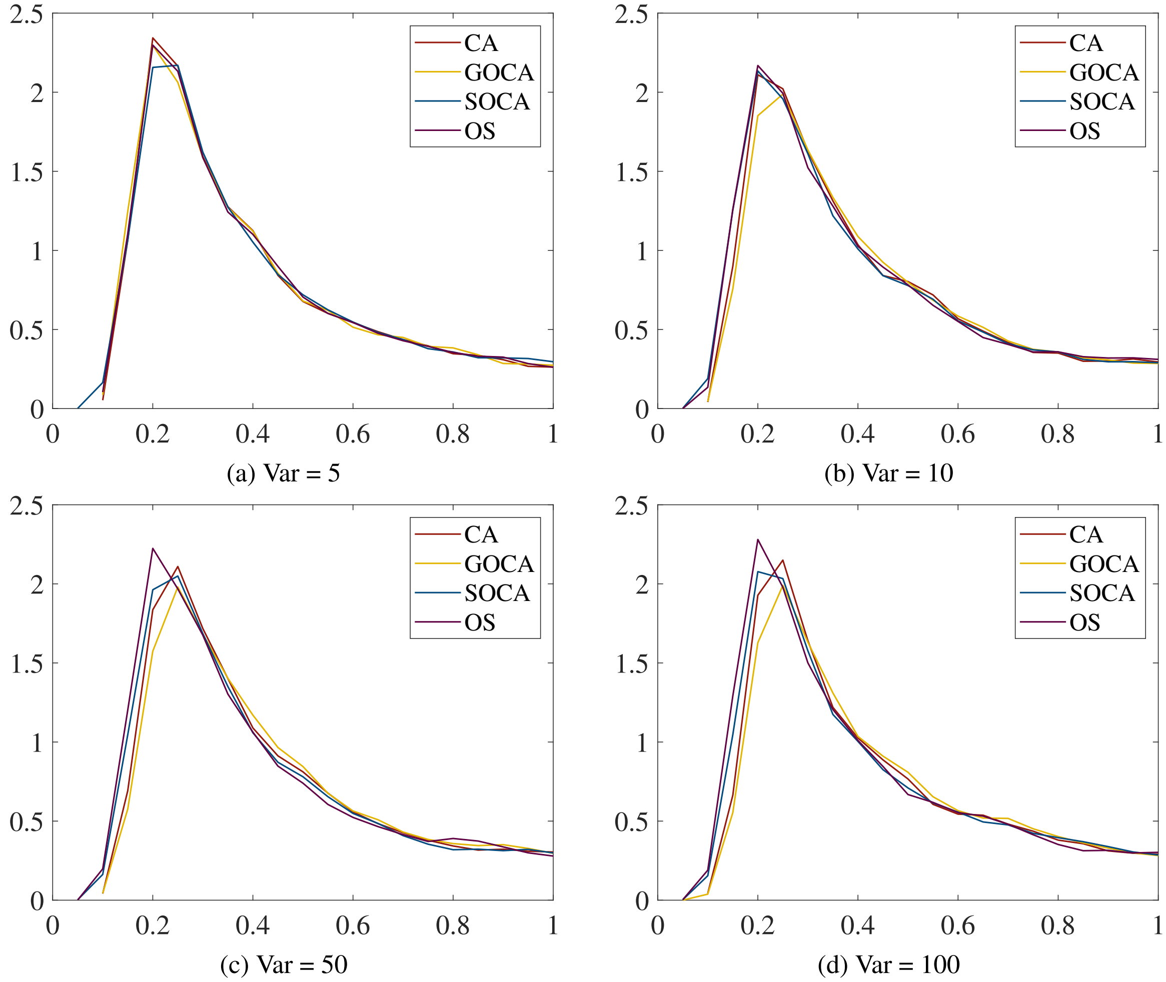

(a) Var = 5 (b) Var = 10 (c) Var = 50 (d) Var = 100

Figure 4.14: Distribution of thresholds calculated by each CFAR detector on simulated range profiles containing lognormal interference

	Var(x) = 5	Var(x) = 10	Var(x) = 50	Var(x) = 100
CA	0.7388	0.7822	0.7930	0.8209
SOCA	0.7452	0.7512	0.7587	0.7841
GOCA	0.7694	0.8159	0.8345	0.8701
OS	0.7399	0.7469	0.7320	0.7519

Table 4.4: Average threshold produced by each detector for different trials of lognormal interference, R_{min} to 50 km

Finally, the curves relating P_D and P_{FA} was found for each CFAR detector in the log-normal and exponential interference trials. When the CFAR detectors processed the clutter patches with scattering coefficients distributed according to a exponential random variable (Figure 4.15), and a lognormal random variable with a variance of 5 (Figure 4.16a), the CA detector performs best. This result is expected and agrees with the previously investigated average threshold metric; the distribution of test statistics resembles an exponential distribution, and thus the CA detector can calculate the lowest threshold from the average value of the test statistics in the CFAR window. As the variance parameter of the lognormal random variable is increased, as seen in Figures 4.16b, 4.16c, and 4.16d, the CA detectors performance is degraded and the OS detector becomes the optimal detector, as it achieves the highest P_D of each detector as the distributions tail grows heavier.

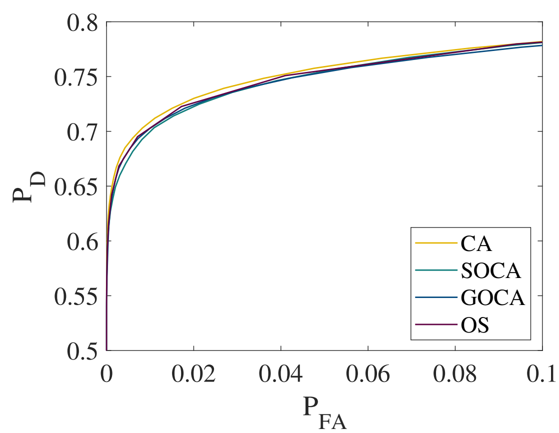

Figure 4.15: CFAR detector performance on simulated exponential interference, $N_r = 6$

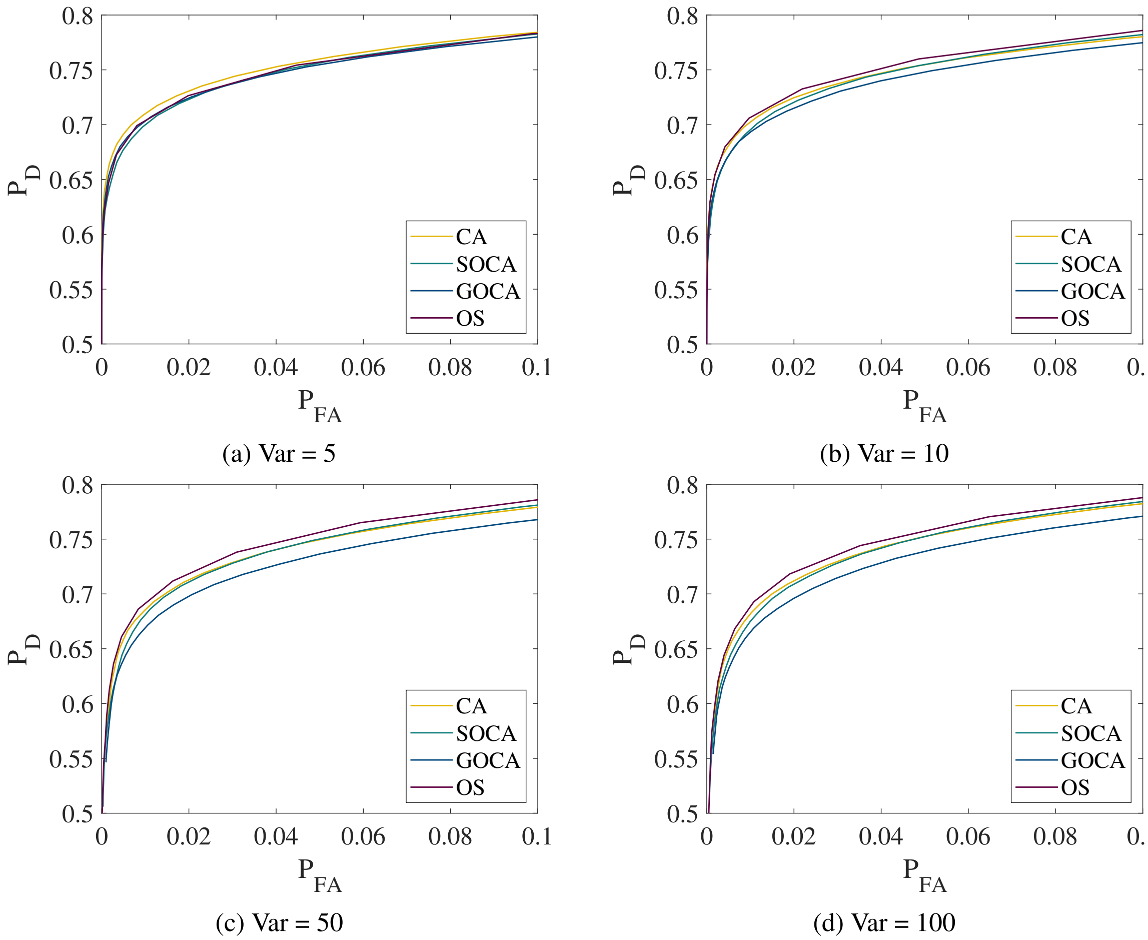

(a) Var = 5 (b) Var = 10

(c) Var = 50 (d) Var = 100

Figure 4.16: CFAR detector performance on simulated lognormal interference, $N_r = 6$

Chapter 5

Conclusion and Future Work

This thesis investigated the impact of nonhomogeneous surface clutter on CFAR detection performance. A simulation was developed to model the operation of a ground-based, mechanically steered surveillance radar, and a representative processing chain was implemented. The stages of the processing chain included matched filtering, clutter filtering, dynamic range compression, and noncoherent integration, all intended to maximize the SINR of target echoes in the test statistics produced by the simulation. Rough surface clutter was modeled to introduce nonhomogeneous interference into the model, and its impact on the output data (and on CFAR detector performance) was analyzed.

The performance of the CA, GOCA, SOCA, and OS CFAR detector algorithms were evaluated using the simulated nonhomogeneous test statistics. The results indicated that the CA, SOCA, and GOCA detectors were sensitive to interference distributed according to a heavy-tailed distribution, such as the lognormal distribution. While the SOCA and GOCA detectors are designed to mitigate statistical outliers of test statistics from the leading or lagging windows, they are unable to counteract outlying test statistics when such values are present in the leading and lagging windows simultaneously. Therefore, the SOCA, GOCA, and CA detectors should not be used as the sole detection technique in real-world surveillance radar systems that anticipate echoes from rough surface clutter.

Among the detectors examined, the OS detector demonstrated the best and most reliable performance. Its design is advantageous because it can counteract statistical outliers from anywhere in the CFAR window to stabilize the false alarm rate and maintain a high probability of detection. As a result of its intelligent design and optimal performance in this study, the OS detector would be a reasonable choice for implementation on a surveillance radar system that may encounter nonhomogeneous sources of interference.

Although the OS detector was determined to be the optimal detector of this study, future work can be done to seek out a detector with improved performance on nonhomogeneous interference. Several CFAR detectors have been suggested in the literature, such as a detector that maintains CFAR when interference follows a two-parameter PDF, an adaptive CFAR that combines that statistically tests if the CFAR window is homogeneous, or machine-learning detectors such as the DeepCFAR and NN-CFAR. The computational complexity of the OS detector is relatively low and does not require any training data, so system designers must consider the trade-offs when choosing a CFAR detector.

References

[1] D. Griffin, *Listening in the Dark*, 2nd ed. Yale University Press, 1958.

[2] M. A. Richards, *Principles of Modern Radar: Basic Principles*, 1st ed. SciTech Publishing, Inc., 2010.

[3] K. Shanmugan and A. Breipohl, *Random Signals: Detection, Estimation and Data Analysis*, 1st ed. John Wiley & Sons, Inc., 1988.

[4] R. M. F.T. Ulaby and A. Fung, *Microwave Remote Sensing: Active and Passive*. Artech House, 1982, vol. II.

[5] A. W. A.V. Oppenheim and S. Nawab, *Signals and Systems*, 2nd ed. Prentice Hall, 1997.

[6] N. Levanon and E. Mozeson, *Radar Signals*, 1st ed. John Wiley & Sons, Inc., 2004.

[7] M. A. Richards, *Fundamentals of Radar Signal Processing*, 3rd ed. McGraw-Hill Education, 2022.

[8] A. Carlson and P. Crilly, *Communication Systems*, 5th ed. McGraw-Hill, 2009.

[9] C. Cook and M. Bernfeld, *Radar Signals: An Introduction to Theory and Application*, 1st ed. Academic Press, 1967.

[10] E. Fowle, "The design of fm pulse-compression signals," *IEEE Transactions on Information Theory*, 1964.

[11] R. Price, "Chebyshev low pulse compression sidelobes via a nonlinear fm," *National Radio Science Meeting of URSI*, 1979.

[12] A. Oppenheim and R. Schafer, *Discrete-Time Signal Processing*, 3rd ed. Prentice Hall, 2009.

[13] N. Levanon, *Radar Principles*, 1st ed. John Wiley & Sons, Inc., 1988.

[14] C. Balanis, *Antenna Theory: Analysis and Design*, 4th ed. John Wiley & Sons, Inc., 2016.

[15] L. Setian, *Practical Communication Antennas with Wireless Applications*, 1st ed. Prentice Hall PTR, 1998.

[16] J. Curlander and R. McDonough, *Synthetic Aperture Radar*, 1st ed. Wiley, 1991.

[17] R. Doviak and D. Zrnic, *Doppler Radar and Weather Observations*, 2nd ed. Dover Publications, 2006.

[18] W. Albersheim, "Closed-form approximation to robertson's detection characteristics," *Proceedings of the IEEE*, 1981.

[19] S. M. Kay, *Fundamentals of Statistical Signal Processing: Detection Theory*. Prentice Hall, Inc., 1998, vol. II.

[20] H. Finn and R. Johnson, "Adaptive detection mode with threshold control as a function of spatially sampled clutter-level estimates," *RCA Review*, 1968.

[21] G. Trunk, "Range resolution of targets using automatic detectors," *IEEE Transactions on Aerospace and Electronic Systems*, 1978.

[22] V. Hansen and J. Sawyers, "Detectability loss due to "greatest of" selection in a cell-averaging cfar," *IEEE Transactions on Aerospace and Electronic Systems*, 1980.

[23] H. Rohling, "Radar cfar thresholding in clutter and multiple target situations," *IEEE Transactions on Aerospace and Electronic Systems*, 1983.

[24] ——, "New cfar-processor based on an ordered statistic," *Proceedings of the IEEE International Radar Conference*, 1985.

[25] N. H. M. Evans and B. Peacock, *Statistical Distributions*, 2nd ed. John Wiley & Sons, Inc., 1993.